Increased West Antarctic ice discharge and East Antarctic stability over the last seven years

Alex S. Gardner[1], Geir Moholdt[2], Ted Scambos[3], Mark Fahnstock[4], Stefan Ligtenberg[5], Michiel van den Broeke[5], Johan Nilsson[1]

[1] Jet Propulsion Laboratory, California Institute of Technology, Pasadena CA 91109

[2] Norwegian Polar Institute, Fram Centre, 9296 Tromsø, Norway

[3] National Snow and Ice Data Center (NSIDC), University of Colorado at Boulder, Boulder CO 80303 USA

[4] Geophysical Institute, University of Alaska Fairbanks, Fairbanks AK 99775 USA

[5] Institute for Marine and Atmospheric research Utrecht (IMAU), Utrecht University, Utrecht, the Netherlands

Correspondence to: Alex S. Gardner (alex.s.gardner@jpl.nasa.gov)

Abstract

Ice discharge from large ice sheets plays a direct role in determining rates of sea level rise. We map present-day Antarctic-wide surface velocities using Landsat 7 & 8 imagery spanning 2013-2015 and compare to earlier estimates derived from synthetic aperture radar, revealing heterogeneous changes in ice flow since ~2008. The new mapping provides complete coastal and inland coverage of ice velocity with a mean error of <10 m yr^{-1}, resulting from multiple overlapping image pairs acquired during the daylit period. Using an optimized flux gate, ice discharge from Antarctica is 1932 ± 38 Gigatons per year (Gt yr^{-1}) in 2015, an increase of 35 ± 15 Gt yr^{-1} from the time of the radar mapping. Flow accelerations across the grounding lines of West Antarctica's Amundsen Sea Embayment, Getz Ice Shelf and Marguerite Bay on the western Antarctic Peninsula, account for 89% of this increase. In contrast, glaciers draining the East Antarctic Ice Sheet have been remarkably stable over the period of observation. Including modeled rates of snow accumulation and basal melt, the Antarctic ice sheet lost ice at an average rate of 186 ± 93 Gt yr^{-1} between 2008 and 2015. The modest increase in ice discharge over the past 7 years is contrasted by high rates of ice sheet mass loss and distinct spatial patters of elevation lowering. This suggests that the recent pattern of mass loss in Antarctica, dominated by the Amundsen Sea sector, is likely part of a longer-term phase of enhanced glacier flow initiated in the decades leading up to the first continent wide radar mapping of ice flow.

1. Introduction

The Antarctic Ice Sheet receives roughly 2000 Gt (~5.5 mm sea-level equivalent) of precipitation each year with >90% of
30 this mass leaving as solid ice discharge to the ocean and the remaining <10% leaving in the form of sublimation, wind-driven snow transport, meltwater runoff, and basal melt. Nearly all recent studies indicate significant mass loss from the Antarctic Ice Sheet that is likely accelerating (*Harig and Simons, 2015; Helm et al., 2014; Martín-Español et al., 2016; McMillan et al., 2014; Rignot et al., 2011b; Shepherd et al., 2012; Velicogna, 2009*). Understanding how this imbalance evolves is critical to provide meaningful projections of sea level change. A major hurdle for improved assessments of the
35 attribution of mass change is the difficulty in resolving continent-wide ice discharge at high precision and accuracy for multiple epochs. This requires circum-Antarctic measurements of surface velocity at fine spatial scale and with sufficient accuracy (~10 m yr^{-1}) to observe regionally coherent changes in flow.

Earlier circum-Antarctic mappings of surface velocity have been based on Synthetic Aperture Radar (SAR) data with
40 incomplete coverage for 1996-2000 (*Jezek et al.*, 2003; *Rignot*, 2006) and near-complete coverage for 2007-2009 (Rignot et al., 2011). Applications of optical imagery for surface velocity mapping have heretofore been limited to more local scales (e.g. *Bindschadler and Scambos*, 1991; *Scambos et al.*, 1992) due to limited sensor capabilities, cloudiness, and too few repeat-image acquisitions. Improvements in sensor technology (particularly in radiometric resolution) and far higher image acquisition rates for Landsat 8, launched in 2013, largely overcome these limitations (*Fahnestock et al.*, 2015; *Jeong and*
45 *Howat*, 2015; *Mouginot et al.*, 2017) and provide the ability to generate near-complete annual mappings of surface velocity with high accuracy (~10 m yr^{-1}).

Here we describe the application of two newly developed and independent feature tracking methodologies (JPL and NSIDC) that we applied to hundreds of thousands of Landsat image pairs covering the entire Antarctic Ice Sheet north of 82.4°S,
50 producing six near-complete mappings of ice sheet surface velocities in both the 2013-14 and 2014-15 austral polar daylight periods. By differencing these velocity fields with the earlier SAR mapping (*Rignot et al.*, 2011a) we resolve changes in ice surface velocity for the 7-year period between circa-2008 and 2015. Velocity changes are then used to estimate ice discharge at the basin scale and its change through time. For the determination of ice discharge we provide a novel approach to defining the cross-sectional area of ice flow (flux gate – Section 2.2) that greatly reduces uncertainties in estimates of ice
55 discharge. By differencing estimates of ice discharge and basal melt rates (*Van Liefferinge and Pattyn*, 2013) from published estimates of the surface mass balance (*van Wessem et al.*, 2016; *van Wessem et al.*, 2014) we are able to estimate the net mass balance of the ice sheet at the basin scale, revealing recent patters of ice sheet imbalance.

2. Methods

2.1 Surface velocity

60 Glacier velocities were determined by feature tracking of matching path-row Landsat image pairs in the panchromatic Band 8 (15 m pixel size) using two independent processing methodologies developed by JPL and NSIDC (Figure 1). Uncertainties in velocities can be as high as 20-30 m yr^{-1} locally but are largely uncorrelated at basin scales (See Appendix A for validation of the velocity fields). All velocity mosaics are freely downloadable from the NSIDC. The details of both methodologies are described here.

65 ### 2.1.1 JPL auto-RIFT

Image pair pixel offsets

The autonomous Repeat Image Feature Tracking (auto-RIFT) processing scheme, developed by JPL (author ASG), was applied to all Landsat 7 and 8 Collection 0 LT1 images acquired over the Antarctic Ice Sheet between August 2013 and May 2016 with 80% cloud cover or less, as indicated in the image metadata. Landsat 7 and 8 panchromatic (Band 8) images (15

70 m pixel size) are preprocessed using a 5 by 5 Wallis operator to normalize for local variability in image radiance caused by shadows, topography and sun angle. Preprocessed image pairs were searched for matching features by finding local normalized cross correlation (NCC) maxima at subpixel resolution using Taylor refinement (*Paragios et al.*, 2006) within a specified search distance. A sparse (1/16 of full search) NCC search was first used to determine areas of coherent correlation between image pairs (only same path-row images used in this study). Results from the sparse search guide a dense search

75 with search centers spaced such that there is no overlap between adjacent template search chips. Highest quality image pairs (< 20% cloud and < 1 year separation) were searched using this approach, with a large search distance centered at zero pixel offset with a 32 by 32 pixel template chip. Spatially resolved statistics (mean and standard deviation of x and y displacements) were used to guide a dense image search of all imagery with 16 x 16 or 32 x 32 pixel template chips depending on expected gradients in surface velocities. Areas of unsuccessful retrievals were searched with progressively

80 increasing template chip sizes of 32, 64, and 128 that increase the signal to noise at the expense of spatial resolution.

Image-pair pixel displacements were calculated from georeferenced images that are in Antarctic Polar Stereographic (EPSG 3031) projection. This introduces scale distortions that increase with distance from the latitude of origin (71° S). We corrected for this scale distortion when converting from pixel displacement to velocity. Velocities and template chip sizes

85 were combined on a common 240 x 240 m grid in Antarctic Polar Stereographic projection (EPSG 3031) with the displacement value taken as the valid displacement determined with the smallest search chip size.

Image geometry between image pairs is highly stable, but images suffer from large *x* and *y* geolocation errors (~15 m). This resulted in good gradients in velocity, but poor absolute velocity. Displacement fields were also contaminated by match

90 blunders (e.g. matching along shadow edges or of surfaces obscured by cloud in one of the two images). Therefore, displacement fields required heavy post-processing to isolate the geophysical signal. This was done by stacking all displacement fields, co-registering them over stable surfaces (time invariant), and filtering based on the interquartile range (*IQR*) determined for each pixel of the displacement stack. All *x* and *y* displacements that fell outside of the range $Q_1 - T \times IQR$ to $Q_3 + T \times IQR$ were culled from the dataset, where Q_1 and Q_3 are the first and third quartile, respectively, and

95 *T* is a scalar that defines the acceptance threshold.

Reference velocity

A reference velocity (Vx_0, Vy_0) field was generated from all individual image-pair velocities. As a first step, gross outliers were removed from the unregistered data by setting *T* equal to 3. Stacked displacement fields were then coregistered by

100 iteratively correcting for the median *x* and *y* velocity difference between individual image-pair velocities and static reference velocity fields (Vx_{ref} and Vy_{ref}) over stable surfaces, stopping after five iterations. For each iteration, coregistered displacements were filtered setting *T* equal to 1.5, and the effective template chip size (resolution of the velocity field) was coarsened for low velocity gradients (<10 m yr^{-1} between adjacent search chips) to minimize high frequency noise while retaining spatial gradients.

105

Initial Vx_{ref} and Vy_{ref} were defined as all grounded ice pixels with median (*M*) velocities < 10 m yr^{-1} and with >100 valid retrievals. Where these conditions were not met, Vx_{ref} and Vy_{ref} were supplemented with Rignot et al. (2011a) velocities < 10 m yr^{-1}. Additionally, all pixels containing exposed rock were initially assigned a Vx_{ref} and Vy_{ref} of 0 m yr^{-1}. Exposed rock was identified using the SCAR Antarctic Digital Database (*Thomson and Cooper*, 1993, Figure 2). The initial template chip size

110 was set to the minimum chip size for which 40% of the valid displacements in the stack were determined using a chip of that size or smaller. After each coregistration of the data, Vx_{ref} and Vy_{ref} were set equal to the error-weighted velocity for those pixels that have velocities < 50 m yr^{-1} and a *Vx* and *Vy IQR* < 40 m yr^{-1}. All pixels containing exposed rock are re-assigned a Vx_{ref} and Vy_{ref} of 0 m yr^{-1}. The uncertainty of each image-pair velocity field was determined as the standard deviation of the residuals to Vx_{ref} and Vy_{ref}. When there were fewer than 320 coregistration pixels within an image pair, the uncertainty was

115 set to the RSS of the pointing uncertainty of each image.

JPL auto-RIFT Annual fields

All image-pair velocities for a given year Y (center date of image-pair > July 15, Y-1 and < July 15, Y) were coregistered using the reference velocity field (Vx_0, Vy_0) where Vx_{ref} and Vy_{ref} were set equal to the error-weighted velocity (Vx_0, Vy_0) for

120 those pixels that have velocities < 50 m yr^{-1} and Vx_0 and Vy_0 *IQR* < 40 m yr^{-1}. Annual weighted averages and quartile velocities were first calculated setting the filter limits based on the quartile ranges of Vx_0 and Vy_0 and setting *T* = 3. Annual weighted averages and quartile velocities were further refined by setting the filter limits based on the quartile ranges of initial annual values and using a more stringent acceptance threshold of *T* = 1.5.

125   Using this approach we calculated four nearly complete Landsat 8 velocity maps: Median (M) and weighted average (W)

velocities for years 2014 and 2015. The 2014 and 2015 velocities were derived from ~100,000 and ~200,000 unique image

pairs, respectively (Figure 1).

2.1.2 NSIDC LISA

NSIDC used the Python image Correlation, PyCorr v1.10, developed for rapid processing on a unix/Macintosh system. The

130   processing algorithm is described in detail by Fahnestock et al. (2015), and is based on image processing schemes described

in Scambos et al. (1992). Accuracy of the displacement determination using 20 x 20 pixel reference image subscenes is

approximately 0.15 pixels. For the Landsat Ice Speed, Antarctica processing (LISA v1.0), we used repeat path-row

acquisitions of Landsat 8 panchromatic band (Band 8) data separated by 16 to 400 days (16-day repeat-orbit multiples),

spanning September 26, 2013 to April 1, 2015. A total of 38,159 image pairs in this timespan were processed. In addition to

135   using a 70% USGS-estimated cloud cover as a criterion for inclusion, we further reduced the number of images processed by

manually selecting those with a high proportion of cloud-free surface coverage. We applied a high-pass filter to the images

of approximately 250 m spatial scale to enhance surface detail and suppress dynamically supported topography, which is

generally fixed in relation to bedrock structures.

140   We then processed the image pairs through the image chip correlation algorithm contained in PyCorr. PyCorr outputs a set

of processed files, which we have named *vx* (x-direction velocity), *vy* (y-direction velocity), *vv* (scalar speed), *corr*

(normalized correlation index of the highest correlation match between the image chips), and *delcorr* (the difference

between the peak match and the second-highest match outside of a 3x3 cell area around the peak). For the LISA v1.0 data

set, we used a reference chip size of 300 x 300 m, producing individual velocity mappings with grid spacing of 300 m and

145   spatial resolution of the velocity field also approximately 300m.

In assembling the mosaic, we reduced noise and eliminated isolated untrustworthy velocity vectors through a series of

comparisons with adjacent vectors. Individual velocity grids are then adjusted for geolocation errors by shifting them to

eliminate observed motion over stationary features (e.g. rock outcrops) and slow-moving areas near ice divides. We then

150   composited the data and resampled the stacked data. We used fairly strong noise and suspect data filtering because there

were a large number of velocity grids available, providing good coverage and high repeat coverage in the final map, even

with a conservative selection of vector grids..

We first eliminated all vectors with a *delcorr* value less than 0.15, since a characteristic of noise values or an uncertain

155   velocity pick is that the main peak correlation index is not significantly higher than other peaks within the search chip grid.

For the remaining unmasked velocities, we examined the difference between the *vv* at the assessed pixel with the eight

surrounding speed values in the speed output grid (*vv*). These surrounding grid locations may or may not have a velocity value (given our noise filtering, above). If a grid location had no output velocity neighbors, it was masked (i.e. not included in the final composite). If only one of the eight neighbor locations populated, we masked the center pixel if the absolute

160   difference between the two *vv* values was greater than 1 m/day. With two neighbors, we required that the center *vv* value be within three standard deviations of the mean of its neighbors, or it was masked. Once the above masking operation was complete, the standard deviation of each 3x3 region was computed, and the center pixel of each region was masked if the corresponding standard deviation is greater than 1 m/day.

165   In compositing the masked velocity, we also sought to adjust false offsets of ice motion due to geolocation errors in the image pairs. This is particularly problematic for closely-spaced pairs (16 and 32 day separations), which in fact were the bulk of the image pairings in our compilation. To correct the effects of imprecise geolocation, we computed three sets of x-y velocity offsets and a corresponding percent coverage associated with that velocity image and that correction algorithm. Each set of offsets and coverages are computed using one of three mask images: a "rock" mask (*vrmsk*), a "near-zero ice

170   velocity" mask (*vzmsk*) and a "low ice velocity" mask (*vlmsk*). The rock mask is derived from Antarctic Digital Database (www.add.scar.org, Figure 2) data. The near-zero velocity mask (areas of <0.055 m d^{-1} or <20 m yr^{-1}) and low velocity mask (areas of <0.11 and >0.055 m d^{-1} or <40 and >20 m yr^{-1}) are both derived from the Rignot et al. (2011a) mapping. Comparison of observed 'velocity' (consisting of true ice velocity and the effect of geolocation offset) with the values in the three mask data sets produces three sets of offset corrections: "rock" offset (*vr*), "near-zero velocity" offsets (*vz*) and "low

175   velocity" offsets (*vl*) offsets.

We compared the mean speed derived from our PyCorr image pair mappings in the three mask regions (areas near rock, areas within near-zero velocity in Rignot et al., 2011a, and areas within low-velocity regions in Rignot et al., 2011a). For the *vr* and vz offsets, we took the mean offset vector of our mapping, given the assumption of zero movement of the rock

180   outcrops in the reference projection. For *vl* we determined the mean *vx* and *vy* magnitudes in the *vlmask* area within the PyCorr image pair mapping and the derived ice motion mean *vx* and *vy* in the same area, and adjusted the measured vectors by the mean mean *vx* and *vy* difference.

Once the rock, near-zero-velocity, and low-velocity corrections were applied, the resulting 300 m/cell velocities for each

185   Landsat scene were bilinearly resampled to the target grid spacing of either 750 m/cell or 125 m/cell. These grids were then composited into the LISA v1.0 mosaic using a weighting scheme that favors the more accurate long-interval velocity determinations (16-day pairs, 0.3 weighting; 32-day pairs, 0.6; 48-day pairs, 0.9; >48-day pairs, 1.0). Additionally, a weighting factor was applied to each cell based on the mean *corr* and *delcorr* values, favoring the highest measurement quality velocity determinations. The velocity grids were then stacked and combined in a weighted average scheme. The

190   number of image pairs in the LISA v1.0 grid ranges from ~10 to over 200 (Figure 1).

2.2 Flux gates

Estimation of ice flux from measurements of surface velocity requires knowledge of the vertical density profile, flow cross-sectional area (flux-gate), and an assumption of the relationship between surface and depth-averaged velocity. The most

195   accurate estimates of ice thickness come from radio-echo sounding (RES) measurements, but RES data only exist for about 19% of the ice sheet grounding line. For the calculation of discharge, we choose to compromise proximity to the grounding line for inclusion of more upstream RES data and for avoiding glacier shear-zones with poorly constrained velocities. We do so by modifying the best-known grounding line to go inland of major shear zones and to follow nearby RES flightlines from which valid ice thickness data can be extracted. We prioritize the nearest and most recent RES data available from seven

200   freely available data sets (Figure 3 and Table 1). For flux gates with no RES data within 1 km distance, ice thickness values are extracted by bilinear interpolation from the ice-thickness grid of Huss and Farinotti (2014) over the Antarctic Peninsula and Bedmap-2 (*Fretwell et al.*, 2013b) for the rest of Antarctica. We generate three alternative flux gates: a grounding-line flux gate (*GL0*), based on a synthesis of mappings of the grounding line; a grounded-ice set of flux gates near upstream of the grounding line improved by following RES profiles (*FG1*); and a flux gate outline based solely on RES profiles in

205   favourable positions (*FG2*).

GL0 is a best-assessment grounding line from a synthesis of incomplete data (53%, *Rignot et al.*, 2011a), a Landsat-based grounding line aided by flexure data from ICESat laser altimetry (41%, *Bindschadler et al.*, 2011) and two MODIS-based grounding line products from 2003 and 2009 (2%, *Haran et al.*, 2014; *Scambos et al.*, 2007). Various other data sources

210   were also employed (4%) and are described in more detail by Depoorter et al. (2013). Since then, it has been updated by more recent grounding line mappings in the Amundsen Sea region (*Rignot et al.*, 2014; *Rignot et al.*, 2011b) and for the Totten Glacier in East Antarctica (*Li et al.*, 2015; *Rignot et al.*, 2013); two highly dynamic regions with considerable ice fluxes and changes in grounding line position. Ice thickness was mainly extracted from the gridded products of Bedmap-2 (67%) and the Antarctic Peninsula (9%), but also a considerable amount of RES data that were within 1 km (applied

215   threshold) of the grounding line (19%). For that, we also considered grid cells in Bedmap-2 that have been derived directly from RES data (7%), as indicated in a data coverage mask. These thickness values have a much lower uncertainty (mean 68 m) than the interpolated thicknesses in areas not covered by RES (mean 168 m). Due to this high uncertainty in interpolated areas, we only used *GL0* for definition of the grounding line and for comparative purposes.

220   *FG1* is a modified version of *GL0* that follows RES flightlines (Figure 3) or Bedmap-2 data cells that are in the vicinity of the grounding line. Whether or not to divert from the grounding line in favor of RES profiles was determined ad hoc rather applying a strict distance threshold. Long, continuous RES profiles further apart were more likely to be followed than short, scattered RES data closer to the grounding line. In general, the modified parts of *FG1* are within a few tens of kilometers from the GL0, and even less so in the Amundsen and Bellingshausen Sea coasts and the Filchner-Ronne ice shelf regions

225   where RES flightlines are often aligned with the grounding line. Almost all of these important regions are covered by RES
data in *FG1*, and for Antarctica as a whole the RES coverage is 42% (Table 1). We found that *FG1* was the most suitable
flux gate line for estimating changes in ice discharge due to its close proximity to the grounding line and high coverage of
RES data.

230   *FG2* is a further modified version of *FG1* that further prioritizes RES flightlines over proximity to the grounding line around
the entire continent. Only slight modifications were made in regions like the Amundsen and Bellingshausen Sea coasts, the
Filchner-Ronne ice shelf and Dronning Maud Land for which many near-grounding line RES data exist, but for parts of East
Antarctica and along the Transantarctic Mountains, the modification can be several hundred kilometers (Figure 3). The total
coverage of RES data along FG2 is 96% (Table 1). We used this flux gate line to estimate absolute discharge for the ice
235   sheet, but not for assessing temporal changes in discharge, because they are often most pronounced near the grounding line
that is better sampled by *FG1*.

The average point spacing along the three flux gate lines is 198-265 m, with a maximum spacing of 400 m to ensure
sufficiently dense sampling of ice thickness and surface velocity for ice flux calculations (see Appendix A for a detailed
240   discussion of resolution dependent errors in flux calculations). This makes a total of between 132,300 and 177,600 flux
nodes for each of the three flux gate lines and a total length of between 26,200 km (*FG2*) and 45,500 km (*GL0*) around the
continent. Flux gate points without RES data and within the rock mask of the SCAR Antarctic Digital Database (<4%,
Thomson and Cooper, 1993, Figure 2) were assigned a zero ice thickness. Since the thickness data were provided as physical
ice thicknesses, we subtracted modelled average (1979-2015) Firn Air Content (FAC – see Section 2.5) to obtain ice
245   equivalent thicknesses, assuming ice has a density of 917 kg m^{-3}, relevant for ice flux calculations.

For further analyses, we also extracted point attributes for source data and year, surface elevation, firn air content and all
available thickness data. Histograms of ice thickness, uncertainties in ice thickness, date of thickness measurement, Firn Air
Content, uncertainty in Firn Air Content, surface velocity, ice thickness change rate, and uncertainty ice thickness change
250   rate for all three flux gates are shown in Figure 4. Flux gates and extracted ancillary data are provided as SI.

2.3 Ice Discharge

We calculate ice flux (*F*) by multiplying the component of the measured surface velocity that is normal to the flux gate
cross section (*V*) by the width (*W*) and ice-equivalent thickness (*H*) at each flux node (*i*) and summing:

255

$$F = \sum_{i=1}^{nn} V_i W_i H_i$$

where nn is the number of nodes at which ice flux is calculated. Ice discharge (D) at the grounding line of the ice sheet corresponds to F for the $GL0$ flux gate and to $F + SMB + dV_{dyn}/dt$ for the $FG1$ and $FG2$ flux gates. SMB is the unmeasured flux due to a positive surface mass budget of the area between the flux gate and the grounding line and is estimated from

260 RACMO2.3 climatology (1979-2015, see Section 2.4). dV_{dyn}/dt is the unmeasured flux due to ice flow convergence/divergence between the flux gate and the grounding line, which we refer to as the dynamic volume change. This is accounted for by assuming that firn corrected CryoSat-2 elevation change rates (Section 2.6) measured over ice moving at >200 m yr^{-1} that lies between the flux-gate and the grounding line can be attributed to dynamic volume change. Rates of volume change in 2008 and 2015 were extrapolated using the measured acceleration in the rate of elevation change

265 over the period of CryoSat-2 data (2011-2015). Measured dynamic volume loss is considered to increase total discharge and visa versa. Uncertainty in the dynamic volume change is taken to be 0.1 m yr^{-1} times the area between the grounding line and the flux gate having a surface velocity >200 m yr^{-1} or 30% of the magnitude of the estimated dynamic volume change, whichever is larger.

270 Calculation of discharge is highly sensitive to the definition of the flux gate and to any vertical gradient in the ice flow. When calculating ice flux, we assume that there are no vertical gradients in ice velocity. This assumption introduces a small positive bias (< 0.4%) but is negligible relative to other sources of error. See Appendix A the calculation of the expected vertical gradient in ice velocity. One known issue is the systematic underestimation of ice flux with the coarsening of the resolution of the basal topography and/or the surface velocity (Figure 5). This happens because fast-moving ice is

275 concentrated in basal troughs: higher velocities multiplied by larger ice thickness, and lower velocities multiplied by smaller ice thickness, do not equate to average thickness multiplied by average velocity. Therefore, we based our total flux estimates on the $FG2$ flux gate that follows high-resolution RES profiles around almost the entire continent at the expense of proximity to the grounding line.

280 For areas south of the Landsat observation limit, we first calculate the total flux across gates located >82.4°S using the 1997 and 2009 SAR velocity mappings *of Scheuchl et al.* (2012). To determine a representative 2015 flux rate we extrapolate the 2009 estimate assuming the same rate of change in discharge as observed for the 1997-2009 period.

285 Changes in flux (dF) were calculated at all flux gate nodes (i) where both velocity mappings were valid and assumed to be unchanged elsewhere. In our analysis of velocities we found that there were some geocoding issues between the SAR (Rignot et al. 2011) and Landsat velocities, that are most likely due to errors in the elevation model used to convert from radar slant range coordinates to a location on the Earth surface. We also found the SAR velocities unreliable for most of the northwest Antarctic Peninsula, where velocities near the grounding lines of narrow outlet glaciers were unrealistically low and likely the results of interpolation to areas of missing data. To minimize the impact of these artifacts in our flux change

290   analyses, we prescribed areas of zero change in flux along shear margins where changes are expected to be small, and for much of the northwest Antarctic Peninsula (Figure 2). We refer to Appendix A for a comprehensive discussion of the uncertainty quantification.

2.4 Surface Mass Budget (SMB)

Here we estimate SMB for the 2008-2015 period from Regional Atmospheric Climate Model version 2.3 (RACMO2.3)
295   output at a horizontal resolution of 5.5 km for the Antarctic Peninsula (*van Wessem et al.*, 2016) and 27 km elsewhere (*van Wessem et al.*, 2014). In RACMO2.3, SMB is calculated as the total precipitation (from snow and rain) minus total sublimation (directly from the surface and from drifting snow), wind-driven snow erosion, and meltwater runoff. For the six Antarctic Peninsula basins (B1, B23-27), entirely or partially covered by the high-resolution model, we use the 27 km model output for the missing years of 2014 and 2015. For these basins, the 27 km model output was scaled to better agree with the
300   5.5 km output using the delta scaling approach. Uncertainty in SMB is taken to be 20% and is treated as uncorrelated between basins. The reader is referred to the works of van Wessem and others (2014 and 2016) for a thorough discussion of the model setup, model validation and SMB uncertainties.

2.5 Firn Air Content (FAC)

305   To convert volume fluxes to mass fluxes, the depth-averaged ice-sheet density is needed. FAC is a measure of the residual column that would remain if the firn column was compressed to the density of glacier ice, assumed to be 917 kg m^{-3}. We estimate FAC using the firn densification model IMAU-FDM (*Ligtenberg et al.*, 2011; *Ligtenberg et al.*, 2014). IMAU-FDM simulates firn densification by dry compaction and through meltwater processes (percolation, retention and refreezing) and is forced at the surface by three-hourly resolution output of RACMO2.3 (*van Wessem et al.*, 2016; *van Wessem et al.*, 2014):
310   surface temperature, 10-m wind speed, precipitation (solid and liquid), sublimation, wind-driven snow erosion/deposition, and surface melt. The simulation over the entire Antarctic continent (at 27 km grid resolution) covers 1979-2015, while the Antarctic Peninsula simulation (at 5.5 km grid resolution) only covers 1979-2013. Both simulations output FAC at 2-day temporal resolution. The IMAU-FDM is calibrated using 48 depth-density observations from across Antarctica (*Ligtenberg et al.*, 2011), and results have been successfully used to convert satellite altimetry (e.g. *Gardner et al.*, 2013; *Scambos et al.*,
315   2014; *Shepherd et al.*, 2012) and ice thickness measurements (e.g. *Depoorter et al.*, 2013; *Fretwell et al.*, 2013b) into estimates of ice mass change and ice equivalent thickness. Although time-evolving FAC is simulated throughout 1979-2015, we use the climatological average FAC as the most robust correction of our flux-gate thicknesses that are based on source data from many different times, sometimes unknown.

320   Uncertainties in the simulated FAC originate from either the observations used in the IMAU-FDM calibration process, or the RACMO2.3 forcing data. This has been quantified at 10% (SI of *Depoorter et al.*, 2013), composed of measurements errors in the observations of the pinning points in a depth-density profile: surface density, depth of 550 kg m^{-3}-level, and depth of

830 kg m^{-3}-level. The RACMO2.3 uncertainty is primarily caused by the assumption used for model initialization; to initialize the IMAU-FDM, it is assumed that the climate over the past 100-1000 years was equal to the 1979-2013/15

325 average climate (Ligtenberg et al., 2011). Therefore, errors in the climatic forcing during the initialization period have a direct effect on the simulated firn density profile and subsequent *FAC*. Using sensitivity simulations, it was found that a 1% perturbation in accumulation during the initialization period causes a 0.75% error in *FAC*. Similarly, a 1% perturbation in the melt/accumulation ratio results in a 0.27 m error in *FAC*. The melt/accumulation ratio was used instead of the total melt, as the amount of annual snow that melts away in summer (i.e., the ratio between annual melt and annual accumulation)

330 mainly determines how much firn pore space remains rather than the total amount of melt.

Along the ice-sheet grounding-line the mean and standard deviation of FAC are 16.3 ± 6.1 m with associated uncertainties of 3.7 ± 1.0 m. The combined uncertainties of the firn observations and the RACMO2.3 forcing of accumulation and surface melt showed the highest uncertainties on the western side of the Antarctic Peninsula, where high accumulation is combined

335 with high melt. In areas where the modelled FAC uncertainty was higher than the actual FAC, the uncertainty was re-set to the same value as the FAC.

2.6 Surface elevation and elevation change

To account for thickness changes between the times of discharge calculation (2008 and 2015) and to correct for dynamic

340 volume change between the flux gate and the grounding line, we use surface elevation rates estimated from CryoSat-2 radar altimetry between January 2011 and January 2015 (Figure 6). CryoSat-2 elevations were derived from the ESA L1c product using the methodology by Nilsson et al. (2016) for the time period of January 2011 to January 2015 over the Antarctic Ice Sheet. For each CryoSat-2 observation mode (LARM and SARIn), the derived surface elevations were separated into grounded and floating ice using the grounded and floating ice definitions from Depoorter et al. (2013) gridded to a 240 m in

345 stereographic (EPSG: 3031) projection. Geophysical range corrections were applied to all data according to Bouzinac (2015). For floating ice, the tidal corrections (ocean tide and ocean loading) were replaced with values generated from the CATS2008 tidal model (*Padman et al.*, 2008).

Surface elevation changes and rates of acceleration were generated using the surface fit method, described in Nilsson et al.

350 (2016), onto a 1 km polar-stereographic grid (EPSG: 3031) for each mode. The derived elevation change distribution was edited to remove solutions with a magnitude larger than ±15 m yr^{-1}, similar to the approach taken by Wouters et al. (2015). The edited data was then interpolated onto a 1 km grid using the weighted average of the 16 closest grid points, weighted by their standard error from the least squares solution and distance. The standard error of the rate of change is assumed to be indicative of the formal error of each measurement. No correction for potential trends in FAC and glacial isostatic

355 adjustment are applied, which may cause surface elevation rates to deviate from ice-equivalent thickness rates.

2.7 Mass Budget

To assess the net ice sheet mass budget during the 2008-2015 period, we combine our new estimates of discharge (Section 2.3) with estimates of surface mass budget (Section 2.4) and basal melt rates (*Pattyn*, 2010; *Van Liefferinge and Pattyn*, 2013). Discharge and surface mass budget for the northern Antarctic Peninsula (B25-26) are highly uncertain and only included for reference in Table 2. The complex basal topography, narrow glacial valleys, and highly crevassed ice, make interpretation of the bed reflection in radar data difficult in this region. Estimating the surface mass budget is equally challenging with large inter-annual variability and steep spatial gradients in both precipitation and melt due to extreme surface topography over a large latitudinal range. For B25-26, we therefore rely on net mass budgets determined from glacier elevation changes within the 2003-2011 period that we update with estimated discharge changes for 2008-2015 (Scambos et al., 2014; Berthier et al., 2012; Shuman et al., 2011). A full discussion of the updated Antarctic Peninsula mass budget estimate is provided in Appendix B.

3 Results

3.1 Changes in surface velocity and ice discharge

By combining uncertainties of ice velocity and its relation to depth-averaged velocity, ice thickness, dynamic volume change and SMB for each flux-gate configuration, we estimate a total discharge uncertainty of 5.6% for *GL0*, 4.4% for *FG1*, and 2.0% for *FG2*. The lower uncertainty for *FG2* is due to the extensive use of RES data for ice thickness along the flux gate (Figure 4). Hence, we use *FG2* in combination with the Landsat velocity field to estimate total discharge. Obtaining continent-wide discharge for ~2008 using the SAR-based velocity field (*Rignot et al.*, 2011a) at the *FG2* flux gate is not possible due to data gaps inland of the grounding line. Instead, we estimate discharge change between the 2008 and Landsat mappings at *FG1*, and then subtract that from the Landsat estimate of discharge to obtain a total estimate for 2008. This approach reduces the impact of ice thickness errors at *FG1* since they get scaled by velocity differences rather than by velocity magnitudes that are typically much larger. Thickness changes at *FG1* and changes in the rate of dynamic volume change between *FG1* and the grounding line 2008 and Landsat mappings were accounted for in the estimates of discharge change using the derived CryoSat-2 elevation change rates for 2011-2015 (see Section 2.6). Rates of volume change in 2008 and 2015 were extrapolated using the measured acceleration over the 2011-2015 period. Calculating flux in this way reduced the uncertainty in the total flux estimate generated from SAR velocities from 90 Gt yr^{-1} to 41 Gt yr^{-1}, a 54% reduction in uncertainty. Estimated changes in ice flux between SAR and Landsat velocity mappings are shown Figure 6. The good agreement between mappings gives us strong confidence in our results. For brevity, we only discuss results from the 2015 JPL mappings hereafter.

3.1.1 Amundsen Sea

For the B21 and B22 catchments, containing Pine Island, Thwaites, Haynes, Pope, Smith, and Kohler glaciers (Figure 7), we find a 6% increase in ice discharge or 17 ± 4 Gt yr^{-1} (Table 2). This implies an average discharge increase of 2.4 Gt yr^{-2} for 2008-2015 that is considerably lower than the 6.5 Gt yr^{-2} previously estimated for 1994-2008 (*Mouginot et al.*, 2014),

390   indicating a recent slowing in the rate of acceleration. Pine Island and Thwaites glaciers both show clear signs of persistent dynamic drawdown, with velocities increasing by >100 m yr^{-1} up to 80-100 km inland from the grounding line (Figure 8). East Kohler and Smith glaciers also show extensive speedups throughout their length, with increases of >100 m yr^{-1} reaching more than 40 km inland likely driven by increased ocean melt rates and subsequent grounding line retreat (*Khazendar et al.*, 2016; *Scheuchl et al.*, 2016). Patterns of velocity change for Pope and Kohler glaciers are more complex,

395   with slowing of up to 100 m yr^{-1} near the grounding line and increased speed by ~50 m yr^{-1} upstream reaching 40-80 km inland. This pattern of change is suggestive of an earlier period of dynamic drawdown that is slowly propagating inland contrasted by more recent deceleration near the grounding line. Glaciers feeding the Getz and Sulzberger ice shelves (B20; including Berry, Hull, and Land Glaciers) increased in speed by 10 to 100 m yr^{-1} at their grounding lines, increasing discharge by 6% (Table 2).

400   ### 3.1.2 Bellingshausen Coast

Localized accelerations of 50-200 m yr^{-1} are observed near grounding lines for several of the major glaciers along the Bellingshausen Coast (B23 and B24) including the Ferrigno, Fox, and Alison ice streams and glaciers feeding into the southern George VI Ice Shelf. Despite some areas of flow acceleration, increases in discharge are highly localized. For many glaciers, the flux gate cross-section is decreasing from regional thinning, resulting in negligible changes in discharge. This

405   result is unexpected, but with high certainty, as this region has experienced high rates of ice shelf thinning (*Paolo et al.*, 2015) and grounding line retreat (*Christie et al.*, 2016), both of which were inferred to have resulted in accelerated dynamic thinning that contributed to a 56 ± 8 Gt yr^{-1} increase in the rate of mass loss that began around 2009 and persisted until at least April 2014 (*Wouters et al.*, 2015). From our analysis we conclude that any changes in discharge contributing to observed rates of thinning must have occurred prior to the SAR mapping of ice velocities.

410   ### 3.1.3 Northern Antarctic Peninsula

Along the west coast of the North Antarctic Peninsula (B25) glaciers feeding into Marguerite Bay (Seller and Prospect) sped up by 400-800 m yr^{-1} at their grounding lines, the largest speedup of all Antarctic glaciers, with an increase of >100 m yr^{-1} reaching 10-15 km upstream. The majority of the west-coast glaciers to the north of Marguerite Bay are not sufficiently sampled in the earlier SAR mapping and are assumed to be unchanged between 2008 and 2015 (Figure 2). Along the east

415   coast of the northern Antarctic Peninsula (B26) most glaciers feeding into the former Larsen A and B ice shelves that collapsed in 1995 and 2002, respectively, have either not changed significantly or show signs of slowing near their

grounding lines (Wuite et al., 2015), with the exception of Leppard and Flask Glaciers. These two glaciers have sped up by 50-100 m yr^{-1} at their grounding lines, likely in response to reduced ice shelf buttressing and a resulting ~200 m yr^{-1} speedup of the abutting Scar Inlet Ice Shelf, in agreement with the findings of Khazendar et al. (2015). Overall, this region shows a

420 modest increase in ice discharge of 5 ± 6 Gt yr^{-1}, most of which comes from the glaciers flowing into Marguerite Bay. Small changes in rates of discharge between periods are in good agreement with constant rates of RACMO-derived surface mass budget and mass changes derived from GRACE data (Appendix B).

3.1.4 Ice Streams feeding large ice shelves

Our analysis suggests a 5-20 m yr^{-1} slowdown of a broad region upstream of both Bindschadler and MacAyeal Ice Streams,

425 which feed the Ross Ice Shelf. Ice streams feeding the Ronne-Filchner Ice Shelf show heterogeneous changes with slowing of 15 – 40 m yr^{-1} upstream of the Rutford and Evans ice stream grounding lines and ~20 m yr^{-1} speed up of the Slessor Ice Stream. Slowing in the Rutford Ice Stream is consistent with the slowing observed between 1997 and 2009 (Scheuchl et al., 2012), but the apparent increase in velocity of the Slessor Ice Stream is of equal magnitude but of opposite sign to the changes observed between 1997 and 2009 (Scheuchl et al., 2012). Further to the east, the Stancomb-Wills Glacier increased

430 in speed by 20-40 m yr^{-1}, just upstream of grounding line, with glaciers feeding the Riiser-Larsen, Fimbul and Amery ice shelves showing little change. Overall, changes in surface velocity along groundling lines of ice streams and glaciers feeding the major ice shelves of East and West Antarctica have not been large enough to significantly impact the net ice discharge for their respective basins (Table 2).

3.1.5 East Antarctic glaciers

435 Ice discharge has remained remarkably stable for the East Antarctic glaciers, particularly along the coasts of Dronning Maud Land and Enderby Land. These basins (B5-B8) showed very little change in ice discharge. The region to the west of Law Dome, including Underwood and Bond glaciers, shows evidence of some increased flow speed and ice discharge. However, the much larger Totten Glacier and the tributaries of the Moscow University Ice Shelf (B13) that drain a large fraction of the East Antarctic Ice Sheet show localized areas of ice speed variations but little change in discharge (Figure 1). This result is

440 consistent with recent findings of Li et al. (2016) showing that the Totten Glacier increase in velocity between 2001 and 2007, likely in response to elevated ocean temperature, but has been relatively stable since.

3.1.6 Antarctic Discharge

In total we estimate that between the SAR and Landsat velocity mappings, the Antarctic Ice Sheet increased its solid ice discharge to the ocean from 1897 ± 41 yr^{-1} to 1932 ± 38 yr^{-1}. This represents a 35 ± 15 Gt yr^{-1} increase in total discharge

445 between 2008 and 2015. 79% of the increases in discharge concentrated to glaciers flowing into the Amundsen Sea and another 11% coming from glaciers flowing into Marguerite Bay. Breaking it down to the main ice-sheet regions, the discharge of the West Antarctic Ice Sheet (B1, B18-23) increased by 29 ± 8 Gt yr^{-1} and the Antarctic Peninsula (B24-27) by

7 ± 6 Gt yr^{-1}, representing a 4% and 3% increase in discharge, respectively. The discharge of the East Antarctic Ice Sheet (B2–17) was remarkably stable with a total discharge of 956 ± 30 Gt yr^{-1} and 955 ± 28 Gt yr^{-1} in 2008 and 2015,

450   respectively.

3.2 Changes in net mass balance

For the West Antarctic Ice Sheet, the 2008-2015 net mass budgets were negative for all but two basins (B1 & B18) (Figure 8), summing to a total imbalance of -213 ± 51 Gt yr^{-1} with largest rates of loss collocated with increased glacier velocities along the Amundsen Sea Embayment (B21 and B22) and Getz Ice Shelf (B20). The East Antarctic Ice Sheet is found to have

455   increased slightly in mass at a rate of 58 ± 73 Gt yr^{-1} with largest gains in Dronning Maud (B6) and Enderby Land (B7 and B8) that can be partially attributed to increase in precipitation rate (+28 Gt yr^{-1} relative to 1979-2007 mean) during the study period, which is consistent with earlier findings (*Boening et al.*, 2012; *King et al.*, 2012; *Shepherd et al.*, 2012). For the whole of Antarctica, we estimate an average mass budget of -186 ± 93 Gt yr^{-1} for the 2008-2015 period. Other recent estimates of Antarctic mass change include those derived from CryoSat-2 altimetry of -159 ± 48 Gt yr^{-1} for the period 2010-

460   2013 (*McMillan et al.*, 2014) and -116 ± 76 Gt yr^{-1} for the period 2011-2014 (*Helm et al.*, 2014, assuming density of ice) and a recent estimate from the joint inversion of gravity, altimetry and GPS data of −159 ± 22 Gt yr^{-1} for the period 2010-2013 (*Martín-Español et al.*, 2016). All three studies show near balance to slightly positive mass changes for the East Antarctic Ice Sheet and large losses for the West Antarctic Ice Sheet and the Antarctic Peninsula, all of which agree well with the results presented here when considering uncertainties and differences in study periods.

4 Discussion

465

Areas of accelerated surface velocity (Figure 7) and increased ice discharge are in good agreement with basin-scale assessment of changes in ice flow and ice discharge (*Li et al.*, 2016; *Mouginot et al.*, 2014) and with patterns of ice sheet thinning determined from laser and radar altimetry (*Flament and Rémy*, 2012; *Helm et al.*, 2014; *Pritchard et al.*, 2009). These show broad regions of surface lowering for glaciers feeding into the Amundsen Sea Embayment and Getz Ice Shelf,

470   and rapid drawdown of smaller glacier systems in the Antarctic Peninsula. Glaciers and ice streams feeding major ice shelves were remarkably stable with small heterogeneous changes in velocity. Apparent upstream slowing of Bindschadler and MacAyeal Ice Streams are at the limit of detectability and difficult to interpret. Recent assessments show varying changes in ice stream velocities for this region (*Hulbe et al.*, 2016; *Scheuchl et al.*, 2012), suggesting that measured trends may be influenced by rapid changes in the sub-ice-stream hydrology (*Hulbe et al.*, 2016).

475

Strongly negative net mass budgets are apparent for the West Antarctic Ice Sheet and are largely due to mean rates of ice discharge greatly exceeding rates of snow accumulation. The basin-averaged results (Figure 9) match remarkably well with patterns of pan-Antarctic multi-decadal (1994-2012) changes in ice shelf thickness (*Paolo et al.*, 2015): Mass gains in

Dronning Maud and Enderby Land are collocated with ice shelf thickening; high rates of mass loss from glaciers feeding
480 into the Amundsen Sea are collocated with high rates of ice shelf thinning; and near balance conditions for Wilkes Land
glaciers and basins feeding the Filchner-Ronne, Ross and Amery Ice Shelves are collocated with ice shelves that have
experienced little change in ice thickness over the past two decades. This result further supports the strong link between
oceanic melting of ice shelves and ice sheet mass budget (*Pritchard et al.*, 2012).

485 The link between basin mass budget and change in discharge is less obvious. This is primarily due to differences in
representative periods as mass budgets represent the cumulative imbalance away from equilibrium state while changes in
discharge are only representative of change in discharge between two periods in time, e.g. a glacier can decelerate but still be
discharging ice at a rate that exceeds the surface mass budget minus basal melt. Increased ice discharge from the Amundsen
Sea Embayment and subsequent partial re-stabilization have been attributed to changes in ice shelf buttressing (*Jacobs et al.*,
490 1996; *Macgregor et al.*, 2012) that resulted from increased ice shelf basal melt rates (*Jacobs et al.*, 2011; *Jenkins et al.*,
1997) and more recently to a decrease in ocean melting resulting from changes in the temperature of intermediate depth
waters (*Dutrieux et al.*, 2014). Increased discharge from glaciers feeding into the Getz Ice Shelf is likely in response to rapid
thinning of the ice shelf due to changes in ocean circulation and the depth of warmer modified Circumpolar Deep Water
(*Jacobs et al.*, 2013).

495 **4 Conclusion**

Applying novel feature tracking methods to hundreds of thousands of Landsat image pairs we are now able construct a
detailed and comprehensive record of recent changes in Antarctic-wide ice flow. When combined with optimized flux gate
definitions and an earlier mapping of surface velocity (*Rignot et al.*, 2011a), such measurements allow for accurate
reconstructions of ice discharge and changes in ice discharge through time. Applying these new capabilities, we determine
500 that the Antarctic Ice Sheet discharged 1897 ± 41 yr⁻¹ of solid ice into the ocean in 2008 increasing to 1932 ± 38 yr⁻¹ in 2015
with 79% of the increases in discharge concentrated to glaciers flowing into the Amundsen Sea and another 11% coming
from glaciers flowing into Marguerite Bay. Glaciers and ice streams feeding major ice shelves were remarkably stable with
small heterogeneous changes in velocity. Strongly negative net mass budgets are apparent for the West Antarctic Ice Sheet
and are largely due to mean rates of ice discharge greatly exceeding rates of snow accumulation. The East Antarctic Ice
505 Sheet experienced near-balance conditions with modest gains in Dronning Maud and Enderby Land driven by increased
rates of precipitation.

Over the last decade, it is evident that larger scale changes in discharge are relatively modest (<7% for all basins) compared
to the fractional imbalance between discharge and surface mass budget (up to several tens of percent). This suggests that that
510 the recent pattern of mass loss in Antarctica, dominated by the Amundsen Sea sector, is likely a part of a longer-term phase

of enhanced glacier flow initiated in the 1990s as indicated by satellite records (*Konrad et al.*, 2017; *Mouginot et al.*, 2014) or as early as the 1940s as proposed from sub-ice-shelf sediment records (*Smith et al.*, 2017). Going forward, the ability to frequently measure ice flow at continental scales will give new insights into the dynamic variability and interconnection of these fast-flowing glaciers, as well as the apparent stability of the East Antarctic ice sheet.

515 **Data availability**

All velocity mosaics are available from NSIDC. Grounding lines, flux gates and ancillary data are provided as Supplementary Data.

Author contributions

A.G. devised the study, developed the JPL auto-RIFT software, did all calculations, and wrote the paper. G.M. was
520 responsible for updating the grounding line location and defining the flux gates, he also spent considerable time revising the manuscript after the lead author broke his wrist while snowboarding. T.S. & M.F. produced the LISA velocity fields; S.L. & M.v.d.B. provided modeled FAC and SMB output and J.N. produced surface elevation change rates from CryoSat-2 data. All authors discussed and commented on the manuscript at all stages.

Competing interests

525 The authors declare that they have no conflict of interest.

Acknowledgements

We thank B. Van Liefferinge and F. Pattyn for kindly sharing their modeled estimates of basal melt rates, B. Wouters for helpful discussions regarding Bellingshausen Sea glacier mass changes, A. Khazendar for helping to provide context for observed changes in glacier velocity, I. Joughin for helpful discussion regarding SAR velocities and sharing of data not used
530 in this study, P. Fretwell for providing information on Bedmap-2, and E. Rignot, J. Mouginot, and B. Scheuchl for making their SAR velocities publically available, without which this study would not have been possible. T.S. is deeply appreciative of T. Haran and M. Klinger for all of their hard work creating the NSIDC velocity maps. This work was supported by funding from the NASA Cryosphere program. The research was conducted at the Jet Propulsion Laboratory, California Institute of Technology under contract with the National Aeronautics and Space Administration, and at University of
535 Colorado Boulder and University of Alaska Fairbanks under NASA grant NNX16AJ88G.

References

Allison, I., and G. Hyland (2010), Amery Ice Shelf compiled and merged ice thickness datasets edited by A. A. D. C.-C. Metadata, doi:https://data.aad.gov.au/metadata/records/AIS_thickness_bottom [updated 2014].

540 Bindschadler, R., H. Choi, A. Wichlacz, R. Bingham, J. Bohlander, K. Brunt, H. Corr, R. Drews, H. Fricker, and M. Hall (2011), Getting around Antarctica: new high-resolution mappings of the grounded and freely-floating boundaries of the Antarctic ice sheet created for the International Polar Year, *The Cryosphere*.

Bindschadler, R. A., et al. (2013), Ice-sheet model sensitivities to environmental forcing and their use in projecting future sea level (the SeaRISE project), *J. Glaciol.*, *59*(214), 195-224, doi:10.3189/2013JoG12J125.

545 Bindschadler, R. A., and T. A. Scambos (1991), Satellite-image-derived velocity field of an Antarctic ice stream, *Science*, *252*(5003), 242-246.

Blankenship, D. D., S. D. Kempf, and D. A. Young (2012), IceBridge HiCARS 2 L2 Geolocated Ice Thickness, Version 1, edited, NASA National Snow and Ice Data Center, Boulder, Colorado, USA, doi:http://dx.doi.org/10.5067/9EBR2T0VXUDG [updated 2015].

550 Boening, C., M. Lebsock, F. Landerer, and G. Stephens (2012), Snowfall-driven mass change on the East Antarctic ice sheet, *Geophys. Res. Lett.*, *39*(21), n/a-n/a, doi:10.1029/2012GL053316.

Bouzinac, C. (2015), CryoSat Product Handbook, edited, European Space Agency https://earth.esa.int/documents/10174/125272/CryoSat_Product_Handbook.

Callens, D., K. Matsuoka, D. Steinhage, B. Smith, E. Witrant, and F. Pattyn (2014), Transition of flow regime along a
555 marine-terminating outlet glacier in East Antarctica, *Cryosphere*, *8*(3), 867-875, doi:10.5194/tc-8-867-2014.

Callens, D., N. Thonnard, J. T. M. Lenaerts, J. M. Van Wessem, W. J. Van De Berg, K. Matsuoka, and F. Pattyn (2015), Mass balance of the Sør Rondane glacial system, East Antarctica, *Ann. Glaciol.*, *56*(70), 63-69, doi:10.3189/2015AoG70A010.

Christie, F. D. W., R. G. Bingham, N. Gourmelen, S. F. B. Tett, and A. Muto (2016), Four-decade record of pervasive
560 grounding line retreat along the Bellingshausen margin of West Antarctica, *Geophys. Res. Lett.*, n/a-n/a, doi:10.1002/2016GL068972.

Cuffey, K., and W. S. B. Paterson (2010), *The physics of glaciers*, xii, 693 p., [698] p. of plates pp., Butterworth-Heinemann/Elsevier, Amsterdam ; Boston.

Depoorter, M. A., J. L. Bamber, J. A. Griggs, J. T. M. Lenaerts, S. R. M. Ligtenberg, M. R. van den Broeke, and G. Moholdt
565 (2013), Calving fluxes and basal melt rates of Antarctic ice shelves, *Nature*, *advance online publication*, doi:10.1038/nature12567.

Dutrieux, P., J. De Rydt, A. Jenkins, P. R. Holland, H. K. Ha, S. H. Lee, E. J. Steig, Q. Ding, E. P. Abrahamsen, and M. Schröder (2014), Strong Sensitivity of Pine Island Ice-Shelf Melting to Climatic Variability, *Science*, *343*(6167), 174-178, doi:10.1126/science.1244341.

570 Fahnestock, M., T. Scambos, T. Moon, A. Gardner, T. Haran, and M. Klinger (2015), Rapid large-area mapping of ice flow using Landsat 8, *Remote Sens. Environ.*, doi:http://dx.doi.org/10.1016/j.rse.2015.11.023.

Flament, T., and F. Rémy (2012), Dynamic thinning of Antarctic glaciers from along-track repeat radar altimetry, *J. Glaciol.*, *58*(211), 830-840, doi:10.3189/2012JoG11J118.

Fretwell, P., et al. (2013a), Bedmap2: improved ice bed, surface and thickness datasets for Antarctica, *Cryosphere*, *7*, 375-
575 393, doi:10.5194/tc-7-375-2013.

Fretwell, P., et al. (2013b), Bedmap2: improved ice bed, surface and thickness datasets for Antarctica, *The Cryosphere*, *7*(1), 375-393, doi:10.5194/tc-7-375-2013.

Gardner, A. S., et al. (2013), A reconciled estimate of glacier contributions to sea level rise: 2003 to 2009, *Science*, *340*(6134), 852-857, doi:10.1126/science.1234532.

580 Gogineni, P. (2012), CReSIS Radar Depth Sounder Data, edited, Lawrence, Kansas, USA, doi:Digital Media, http://data.cresis.ku.edu/ [updated 2015].

Haran, T., J. Bohlander, T. Scambos, T. Painter, and M. Fahnestock (2014), MODIS Mosaic of Antarctica 2008-2009 (MOA2009) Image Map, Version 1. , *Boulder, Colorado USA. NSIDC: National Snow and Ice Data Center.* , doi:http://dx.doi.org/10.7265/N5KP8037.

585 Harig, C., and F. J. Simons (2015), Accelerated West Antarctic ice mass loss continues to outpace East Antarctic gains, *Earth Planet. Sci. Lett.*, *415*, 134-141.

Helm, V., A. Humbert, and H. Miller (2014), Elevation and elevation change of Greenland and Antarctica derived from CryoSat-2, *The Cryosphere*, *8*(4), 1539-1559, doi:10.5194/tc-8-1539-2014.

Hulbe, C. L., T. A. Scambos, M. Klinger, and M. A. Fahnestock (2016), Flow variability and ongoing margin shifts on
590   Bindschadler and MacAyeal Ice Streams, West Antarctica, *Journal of Geophysical Research: Earth Surface*, n/a-n/a, doi:10.1002/2015JF003670.

Huss, M., and D. Farinotti (2014), A high-resolution bedrock map for the Antarctic Peninsula, *The Cryosphere*, *8*(4), 1261-1273, doi:10.5194/tc-8-1261-2014.

Jacobs, S., C. Giulivi, P. Dutrieux, E. Rignot, F. Nitsche, and J. Mouginot (2013), Getz Ice Shelf melting response to
595   changes in ocean forcing, *Journal of Geophysical Research: Oceans*, *118*(9), 4152-4168, doi:10.1002/jgrc.20298.

Jacobs, S. S., H. H. Hellmer, and A. Jenkins (1996), Antarctic Ice Sheet melting in the southeast Pacific, *Geophys. Res. Lett.*, *23*(9), 957-960, doi:10.1029/96GL00723.

Jacobs, S. S., A. Jenkins, C. F. Giulivi, and P. Dutrieux (2011), Stronger ocean circulation and increased melting under Pine Island Glacier ice shelf, *Nature Geosci*, *4*(8), 519-523,
600   doi:http://www.nature.com/ngeo/journal/v4/n8/abs/ngeo1188.html - supplementary-information.

Jenkins, A., D. G. Vaughan, S. S. Jacobs, H. H. Hellmer, and J. R. Keys (1997), Glaciological and oceanographic evidence of high melt rates beneath Pine Island Glacier, West Antarctica, *J. Glaciol.*, *43*(143), 114-121.

Jeong, S., and I. M. Howat (2015), Performance of Landsat 8 Operational Land Imager for mapping ice sheet velocity, *Remote Sens. Environ.*, *170*, 90-101, doi:http://dx.doi.org/10.1016/j.rse.2015.08.023.

605 Jezek, K. C., K. Farness, R. Carande, X. Wu, and N. Labelle-Hamer (2003), RADARSAT 1 synthetic aperture radar observations of Antarctica: Modified Antarctic Mapping Mission, 2000, *Radio Science*, *38*(4), n/a-n/a, doi:10.1029/2002RS002643.

Khazendar, A., C. P. Borstad, B. Scheuchl, E. Rignot, and H. Seroussi (2015), The evolving instability of the remnant Larsen B Ice Shelf and its tributary glaciers, *Earth Planet. Sci. Lett.*, *419*, 199-210,
610   doi:http://dx.doi.org/10.1016/j.epsl.2015.03.014.

Khazendar, A., E. Rignot, D. M. Schroeder, H. Seroussi, M. P. Schodlok, B. Scheuchl, J. Mouginot, T. C. Sutterley, and I. Velicogna (2016), Rapid submarine ice melting in the grounding zones of ice shelves in West Antarctica, *Nature Communications*, *7*, 13243, doi:10.1038/ncomms13243
http://www.nature.com/articles/ncomms13243 - supplementary-information.

615 King, M. A., R. J. Bingham, P. Moore, P. L. Whitehouse, M. J. Bentley, and G. A. Milne (2012), Lower satellite-gravimetry estimates of Antarctic sea-level contribution, *Nature*, *491*(7425), 586-589,
doi:http://www.nature.com/nature/journal/vaop/ncurrent/abs/nature11621.html - supplementary-information.

Konrad, H., L. Gilbert, S. L. Cornford, A. Payne, A. Hogg, A. Muir, and A. Shepherd (2017), Uneven onset and pace of ice-dynamical imbalance in the Amundsen Sea Embayment, West Antarctica, *Geophys. Res. Lett.*, *44*(2), 910-918,
620   doi:10.1002/2016GL070733.

Leuschen, C., P. Gogineni, F. Rodriguez-Morales, J. Paden, and C. Allen (2010), IceBridge MCoRDS L2 Ice Thickness, Version 1, edited, NASA National Snow and Ice Data Center, Boulder, Colorado, USA, doi:http://dx.doi.org/10.5067/GDQ0CUCVTE2Q [updated 2015].

Li, X., E. Rignot, M. Morlighem, J. Mouginot, and B. Scheuchl (2015), Grounding line retreat of Totten Glacier, East
625   Antarctica, 1996 to 2013, *Geophys. Res. Lett.*, *42*(19), 8049-8056, doi:10.1002/2015GL065701.

Li, X., E. Rignot, J. Mouginot, and B. Scheuchl (2016), Ice flow dynamics and mass loss of Totten Glacier, East Antarctica, from 1989 to 2015, *Geophys. Res. Lett.*, *43*(12), 6366-6373, doi:10.1002/2016GL069173.

Ligtenberg, S. R. M., M. M. Helsen, and M. R. van den Broeke (2011), An improved semi-empirical model for the densification of Antarctic firn, *The Cryosphere*, *5*(4), 809-819, doi:10.5194/tc-5-809-2011.

630 Ligtenberg, S. R. M., P. Kuipers Munneke, and M. R. van den Broeke (2014), Present and future variations in Antarctic firn air content, *The Cryosphere*, *8*(5), 1711-1723, doi:10.5194/tc-8-1711-2014.

Macgregor, J. A., G. A. Catania, M. S. Markowski, and A. G. Andrews (2012), Widespread rifting and retreat of ice-shelf margins in the eastern Amundsen Sea Embayment between 1972 and 2011, *J. Glaciol.*, *58*(209), 458-466, doi:10.3189/2012JoG11J262.

635   Martín-Español, A., et al. (2016), Spatial and temporal Antarctic Ice Sheet mass trends, glacio-isostatic adjustment, and
         surface processes from a joint inversion of satellite altimeter, gravity, and GPS data, *Journal of Geophysical
         Research: Earth Surface*, *121*(2), 182-200, doi:10.1002/2015JF003550.
         McMillan, M., A. Shepherd, A. Sundal, K. Briggs, A. Muir, A. Ridout, A. Hogg, and D. Wingham (2014), Increased ice
         losses from Antarctica detected by CryoSat-2, *Geophys. Res. Lett.*, *41*(11), 2014GL060111,
640   doi:10.1002/2014GL060111.
         Mouginot, J., E. Rignot, and B. Scheuchl (2014), Sustained increase in ice discharge from the Amundsen Sea Embayment,
         West Antarctica, from 1973 to 2013, *Geophys. Res. Lett.*, *41*(5), 1576-1584, doi:10.1002/2013GL059069.
         Mouginot, J., E. Rignot, B. Scheuchl, and R. Millan (2017), Comprehensive Annual Ice Sheet Velocity Mapping Using
         Landsat-8, Sentinel-1, and RADARSAT-2 Data, *Remote Sensing*, *9*(4), 364.
645   Nilsson, J., A. Gardner, L. Sandberg Sørensen, and R. Forsberg (2016), Improved retrieval of land ice topography from
         CryoSat-2 data and its impact for volume-change estimation of the Greenland Ice Sheet, *The Cryosphere*, *10*(6),
         2953-2969, doi:10.5194/tc-10-2953-2016.
         Padman, L., S. Y. Erofeeva, and H. A. Fricker (2008), Improving Antarctic tide models by assimilation of ICESat laser
         altimetry over ice shelves, *Geophys. Res. Lett.*, *35*(22).
650   Paolo, F. S., H. A. Fricker, and L. Padman (2015), Volume loss from Antarctic ice shelves is accelerating, *Science*,
         348(6232), 327-331, doi:10.1126/science.aaa0940.
         Paragios, N., Y. Chen, and O. D. Faugeras (2006), *Handbook of mathematical models in computer vision*, Springer Science
         & Business Media.
         Pattyn, F. (2010), Antarctic subglacial conditions inferred from a hybrid ice sheet/ice stream model, *Earth Planet. Sci. Lett.*,
655   *295*(3–4), 451-461, doi:http://dx.doi.org/10.1016/j.epsl.2010.04.025.
         Pritchard, H. D., R. J. Arthern, D. G. Vaughan, and L. A. Edwards (2009), Extensive dynamic thinning on the margins of the
         Greenland and Antarctic ice sheets, *Nature*, *461*(7266), 971-975.
         Pritchard, H. D., S. R. M. Ligtenberg, H. A. Fricker, D. G. Vaughan, M. R. van den Broeke, and L. Padman (2012),
         Antarctic ice-sheet loss driven by basal melting of ice shelves, *Nature*, *484*(7395), 502-505,
660   doi:http://www.nature.com/nature/journal/v484/n7395/abs/nature10968.html - supplementary-information.
         Rignot, E. (2006), Changes in ice dynamics and mass balance of the Antarctic ice sheet, *Philosophical Transactions of the
         Royal Society of London A: Mathematical, Physical and Engineering Sciences*, *364*(1844), 1637-1655,
         doi:10.1098/rsta.2006.1793.
         Rignot, E., S. Jacobs, J. Mouginot, and B. Scheuchl (2013), Ice-shelf melting around Antarctica, *Science*, *341*(6143), 266-
665   270.
         Rignot, E., J. Mouginot, M. Morlighem, H. Seroussi, and B. Scheuchl (2014), Widespread, rapid grounding line retreat of
         Pine Island, Thwaites, Smith, and Kohler glaciers, West Antarctica, from 1992 to 2011, *Geophys. Res. Lett.*, *41*(10),
         3502-3509, doi:10.1002/2014GL060140.
         Rignot, E., J. Mouginot, and B. Scheuchl (2011a), Ice Flow of the Antarctic Ice Sheet, *Science*, *333*(6048), 1427-1430,
670   doi:10.1126/science.1208336.
         Rignot, E., I. Velicogna, M. R. van den Broeke, A. Monaghan, and J. Lenaerts (2011b), Acceleration of the contribution of
         the Greenland and Antarctic ice sheets to sea level rise, *Geophys. Res. Lett.*, *38*(5), L05503,
         doi:10.1029/2011gl046583.
         Scambos, T. A., E. Berthier, T. Haran, C. A. Shuman, A. J. Cook, S. R. M. Ligtenberg, and J. Bohlander (2014), Detailed ice
675   loss pattern in the northern Antarctic Peninsula: widespread decline driven by ice front retreats, *The Cryosphere*,
         8(6), 2135-2145, doi:10.5194/tc-8-2135-2014.
         Scambos, T. A., M. J. Dutkiewicz, J. C. Wilson, and R. A. Bindschadler (1992), Application of Image Cross-Correlation to
         the Measurement of Glacier Velocity Using Satellite Image Data, *Remote Sens. Environ.*, *42*(3), 177-186.
         Scambos, T. A., T. M. Haran, M. A. Fahnestock, T. H. Painter, and J. Bohlander (2007), MODIS-based Mosaic of
680   Antarctica (MOA) data sets: Continent-wide surface morphology and snow grain size, *Remote Sens. Environ.*,
         111(2–3), 242-257, doi:http://dx.doi.org/10.1016/j.rse.2006.12.020.
         Scheuchl, B., J. Mouginot, and E. Rignot (2012), Ice velocity changes in the Ross and Ronne sectors observed using satellite
         radar data from 1997 and 2009, *The Cryosphere*, *6*(5), 1019-1030, doi:10.5194/tc-6-1019-2012.

Scheuchl, B., J. Mouginot, E. Rignot, M. Morlighem, and A. Khazendar (2016), Grounding line retreat of Pope, Smith, and
685   Kohler Glaciers, West Antarctica, measured with Sentinel-1a radar interferometry data, *Geophys. Res. Lett.*, *43*(16),
        8572-8579, doi:10.1002/2016GL069287.
Shepherd, A., et al. (2012), A Reconciled Estimate of Ice-Sheet Mass Balance, *Science*, *338*(6111), 1183-1189,
        doi:10.1126/science.1228102.
Smith, J. A., et al. (2017), Sub-ice-shelf sediments record history of twentieth-century retreat of Pine Island Glacier, *Nature*,
690   *541*(7635), 77-80, doi:10.1038/nature20136.
Thomson, J., and A. Cooper (1993), The SCAR Antarctic digital topographic database, *Antarctic Science*, *5*(03), 239-244.
Van Liefferinge, B., and F. Pattyn (2013), Using ice-flow models to evaluate potential sites of million year-old ice in
        Antarctica, *Clim. Past*, *9*(5), 2335-2345, doi:10.5194/cp-9-2335-2013.
van Wessem, J. M., et al. (2016), The modelled surface mass balance of the Antarctic Peninsula at 5.5 km horizontal
695   resolution, *The Cryosphere*, *10*(1), 271-285, doi:10.5194/tc-10-271-2016.
van Wessem, J. M., et al. (2014), Improved representation of East Antarctic surface mass balance in a regional atmospheric
        climate model, *J. Glaciol.*, *60*(222), 761-770, doi:10.3189/2014JoG14J051.
Velicogna, I. (2009), Increasing rates of ice mass loss from the Greenland and Antarctic ice sheets revealed by GRACE,
        Geophys. Res. Lett., *36*(19), L19503, doi:10.1029/2009gl040222.
700   Watkins, M. M., D. N. Wiese, D.-N. Yuan, C. Boening, and F. W. Landerer (2015), Improved methods for observing Earth's
        time variable mass distribution with GRACE using spherical cap mascons, *Journal of Geophysical Research: Solid
        Earth*, *120*(4), 2648-2671, doi:10.1002/2014JB011547.
Wouters, B., A. Martin-Español, V. Helm, T. Flament, J. M. van Wessem, S. R. M. Ligtenberg, M. R. van den Broeke, and
        J. L. Bamber (2015), Dynamic thinning of glaciers on the Southern Antarctic Peninsula, *Science*, *348*(6237), 899-
705   903, doi:10.1126/science.aaa5727.
Zwally, H. J., B. M. Giovinetto, M. A. Beckley, and J. L. Saba (2002), Antarctic and Greenland Drainage Systems, *GSFC
        Cryospheric Sciences Laboratory, at*
http://icesat4.gsfc.nasa.gov/cryo_data/ant_grn_drainage_systems.php. .

710
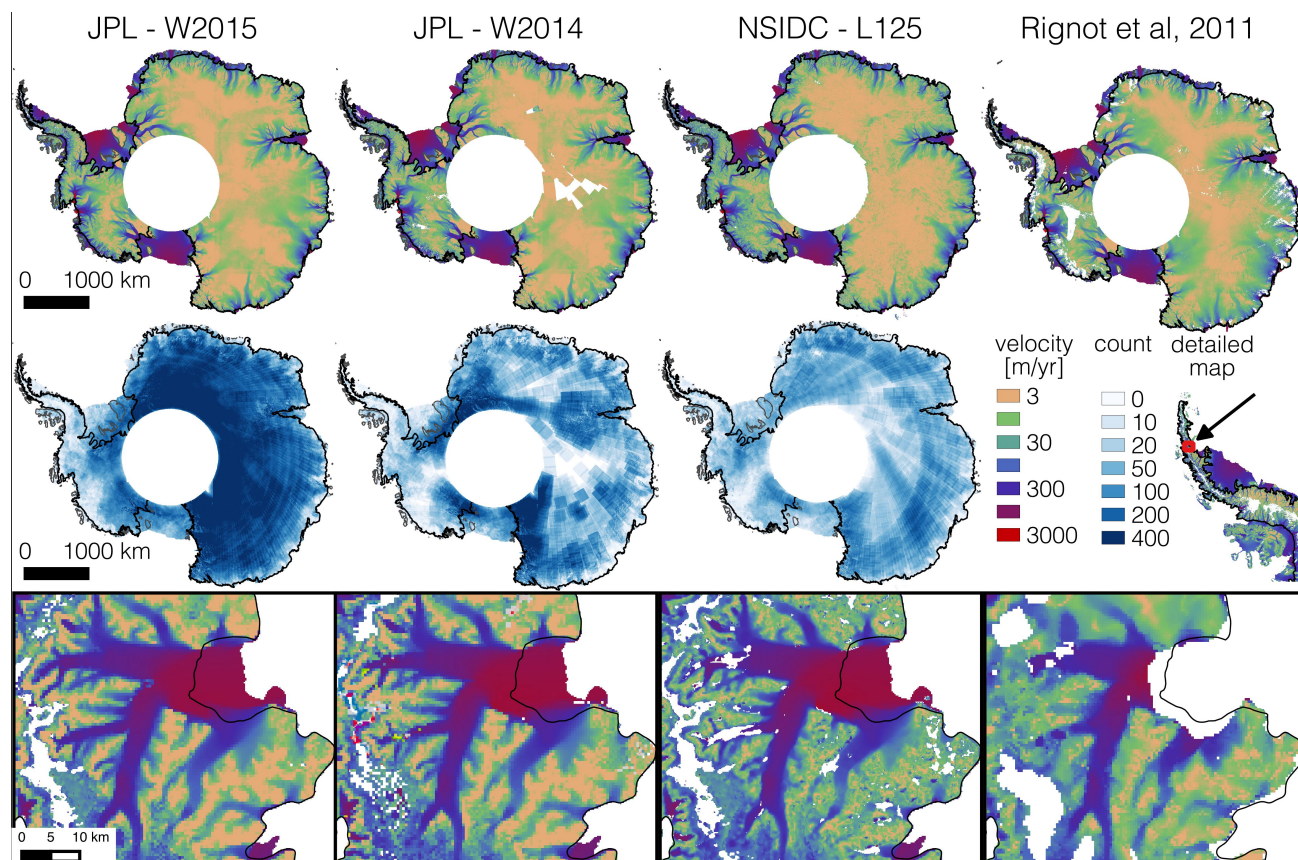
Figures:

Figure 1: Comparison between JPL Weighted Average, NSIDC LISA 125m and Rignot et al. (2011) surface velocities. Top row shows Antarctic-wide velocities, middle row shows the valid image pair velocity counts for Landsat mappings, and bottom row shows close-ups of the Hektoria Glacier, located on the Eastern side of the Antarctic Peninsula for spatial detail.

715
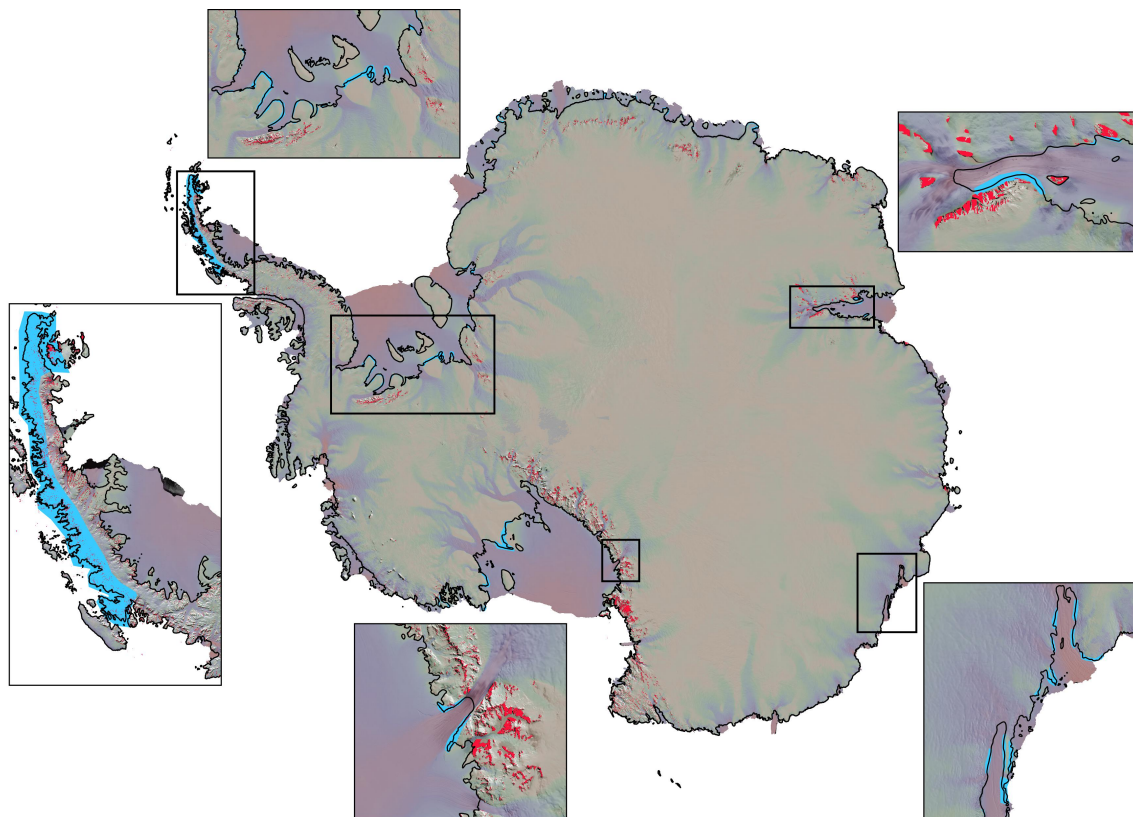
Figure 2: Antarctic Ice Sheet Velocities overlain on the MODIS Mosaic of Antarctica (*Scambos et al.*, 2007). Areas of imposed zero change in velocity are shown in cyan. Areas of prescribed zero surface velocity (rock outcrops) are shown in red as defined according to the Antarctic Digital Database (www.add.scar.org).

720
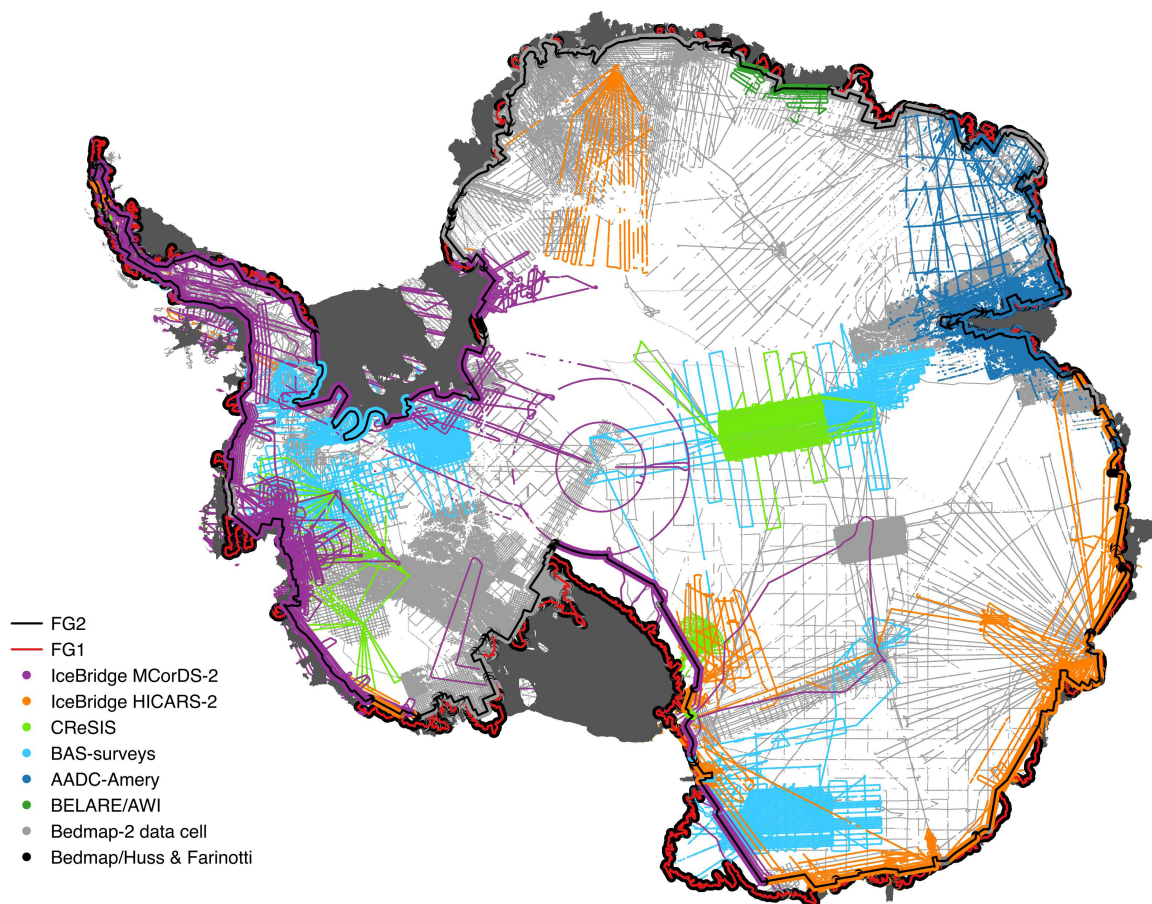
Figure 3: Radio-echo sounding data used to compile flux gates FG1 and FG2. An overview of the use and of each data set and their references are provided in Table 1.
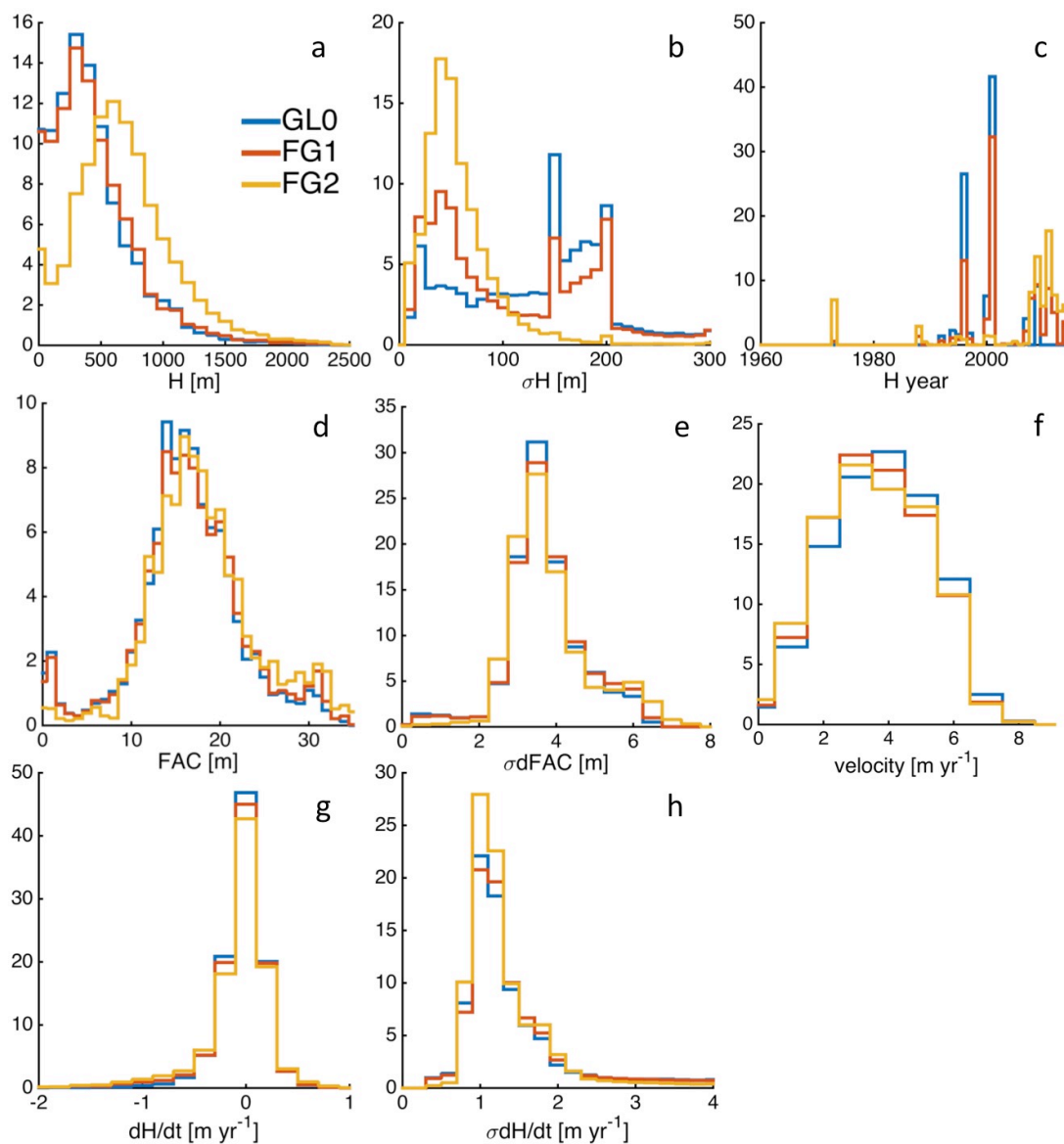
Figure 4: Ice equivalent thickness (a), uncertainty in ice equivalent thickness (b), year of ice thickness measurement (c), Firn Air Content (d), uncertainty in Firn Air Content (e), surface velocity (f), change rate of ice equivalent thickness (g), and uncertainty in change rate of ice equivalent thickness (h) for GL0, FG1 and FG2 flux gates. Y-axis is fraction of nodes by count.
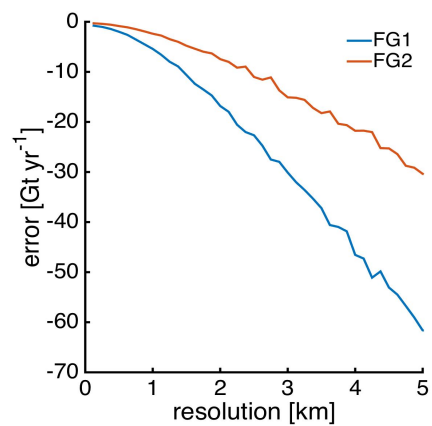
730

Figure 5: Error in total Antarctic discharge (relative to best estimate) when velocity and ice thickness are averaged for increasing along flux gate resolutions prior to computing flux.
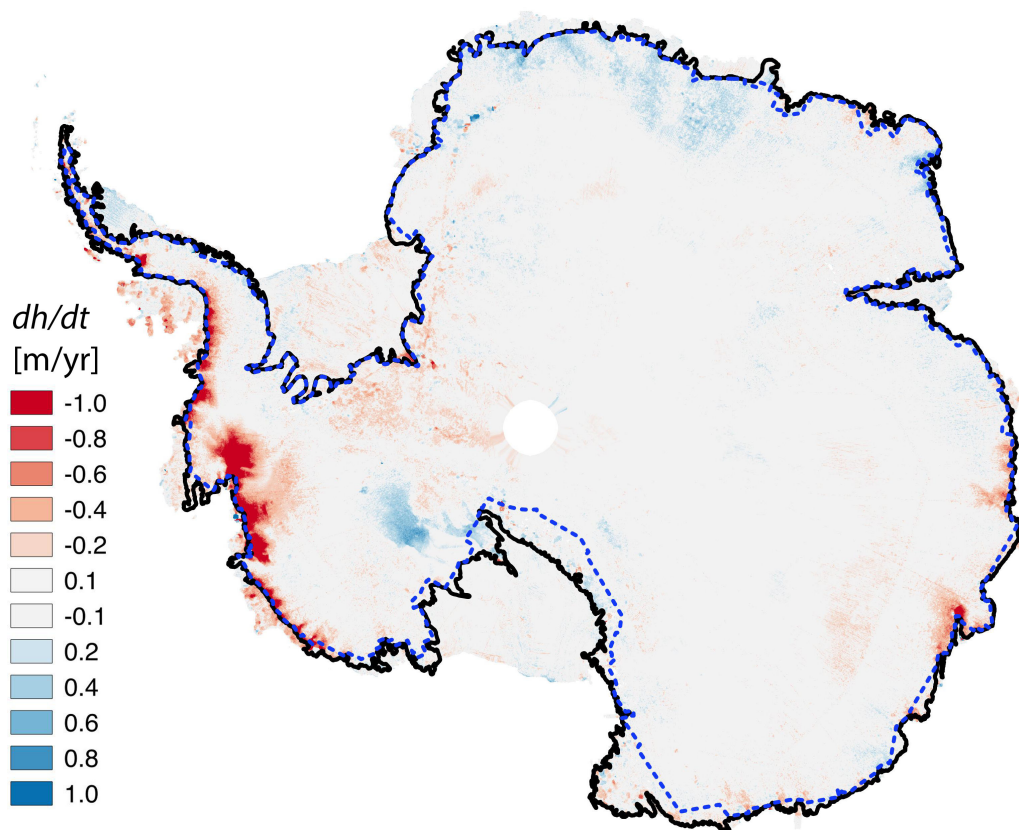
735   **Figure 6: CryoSat-2 surface elevation change for the period 2011 to 2015. Flux gate FG2 shown with blue dashed line and GL0 shown with heavy black line.**

Incomplete basin coverage:
+ Fraction of cross-section assuming constant 1996 and 2009 rate of change: 17 = 62%, 18 = 75%
* Fraction of cross-section assumed unchanged: 2 = 36%, 25 = 75%
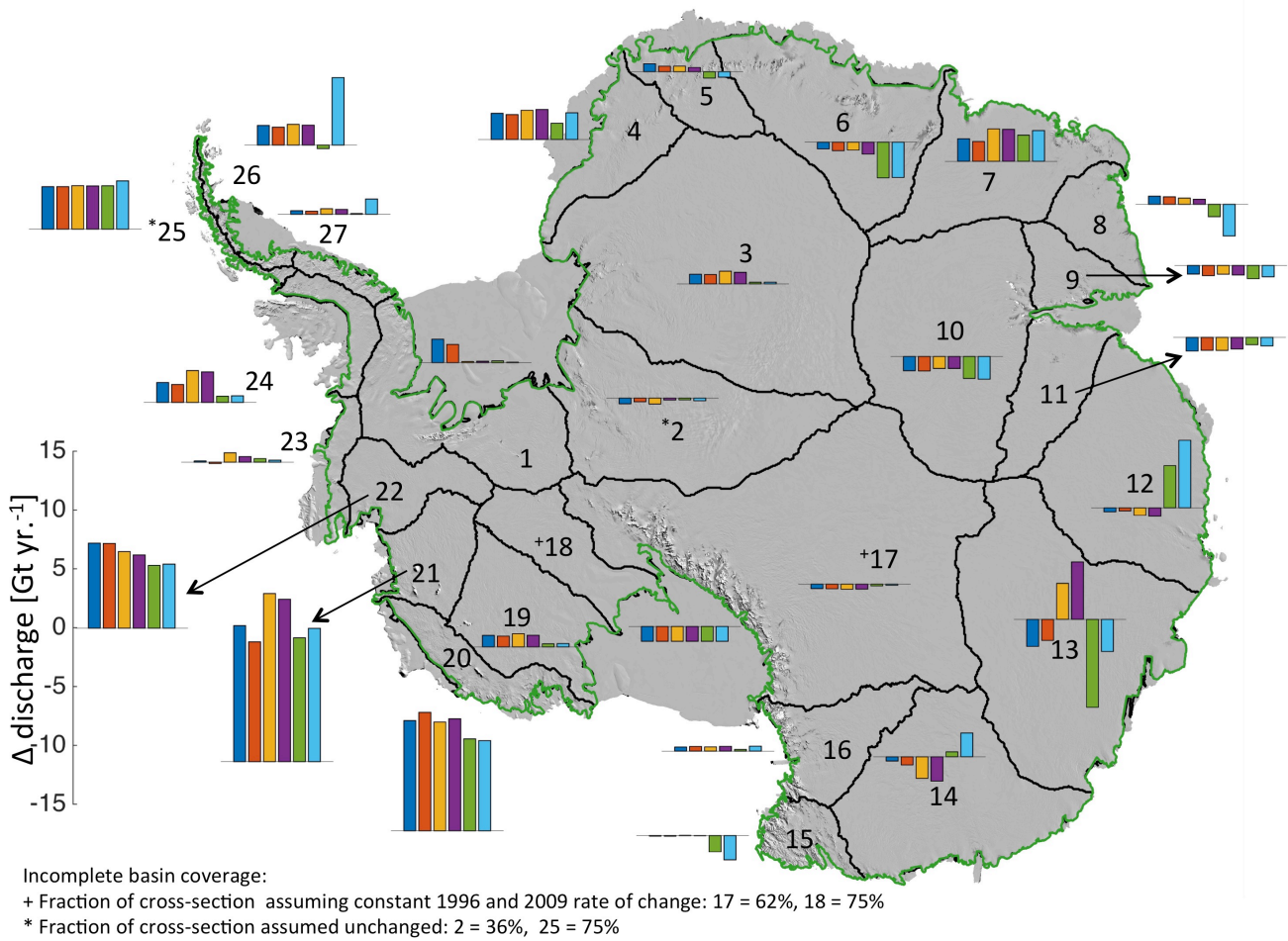
740   **Figure 6: Change in flux across FG1 flux gate (shown with green line, see methods) for the 27 basins defined by Zwally et al. (2002) calculated by differencing the pan-Antarctic SAR mapping of Rignot et al. (2011a, circa-2008) with 6 different Landsat 8 velocity mappings (M14/15 = JPL median of all 2014/15 image pairs, and W14/15 = JPL weighted average of all 2014/15 image pairs. L750 = NSIDC 750 m average of all 2014-15 image pairs, L125 = NSIDC 125 m average of all 2014-15 image pairs. Basins 2, 17, 18 are complimented with differences in 1997 and 2009 SAR velocities poleward of 82.5 degrees south (*Scheuchl et al.*, 2012).**

745
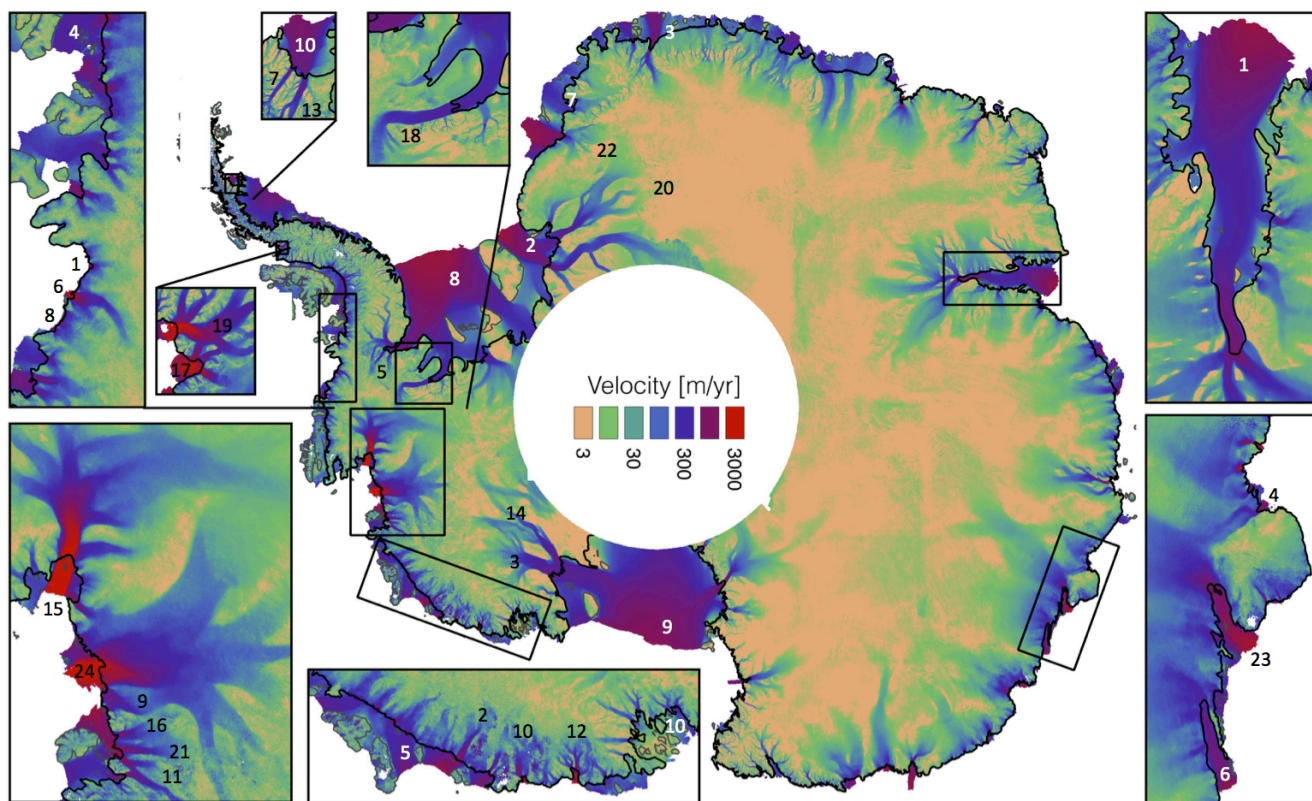
Figure 7: 2015 Antarctic ice sheet surface velocities shown in log-scale determined from feature tracking of >200,000 Landsat image pairs. Glacier and Ice Streams discussed in text labeled with black numbering: (1) Alison, (2) Berry, (3) Bindschadler, (4) Bond, (5) Evans, (6) Ferrigno, (7) Flask, (8) Fox, (9) Haynes, (10) Hull, (11) Kohler, (12) Land, (13) Leppard, (14) MacAyeal, (15) Pine Isl., (16) Pope, (17) Prospect, (18) Rutford, (19) Seller, (20) Slessor, (21) Smith, (22) Stancomb-Wills, (23) Totten, and (24) Twaites. Ice Shelves labeled with white numbering 1 Amery: (2) Filchner, (3) Fimbul, (4) George VI, (5) Getz, (6) Moscow U., (7) Riiser-Larsen, (8) Ronne, (9) Ross, (10) Scar Inlet, and (10) Sulzberger.
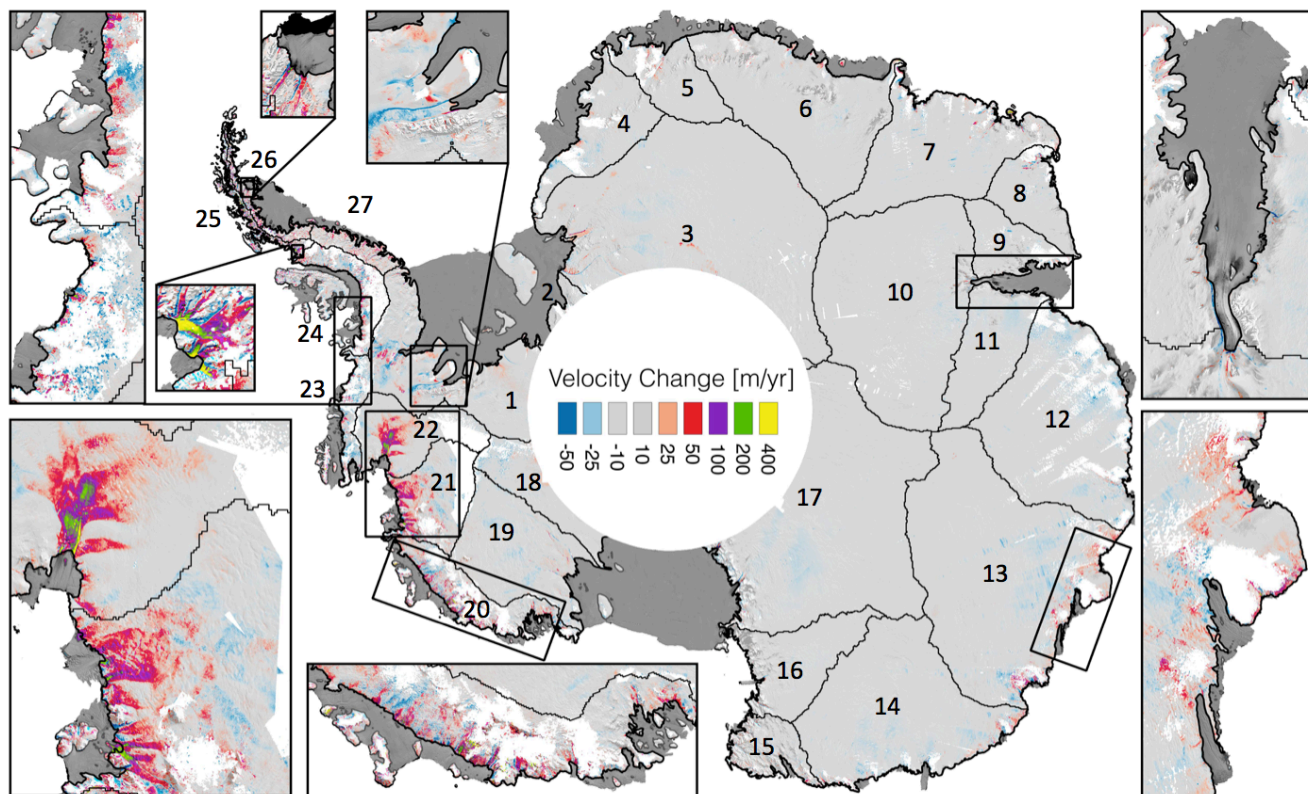
760

Figure 8: Change in surface velocities between date of pan-Antarctic SAR mapping (*Rignot et al.*, 2011a, circa-2008) and new 2015 velocity mapping produced here from feature tracking of Landsat 8 imagery. Change in velocities shown for grounded ice only. Missing data shown in white and the 27 basin boundaries defined by Zwally et al. (2002) are shown in black.

765
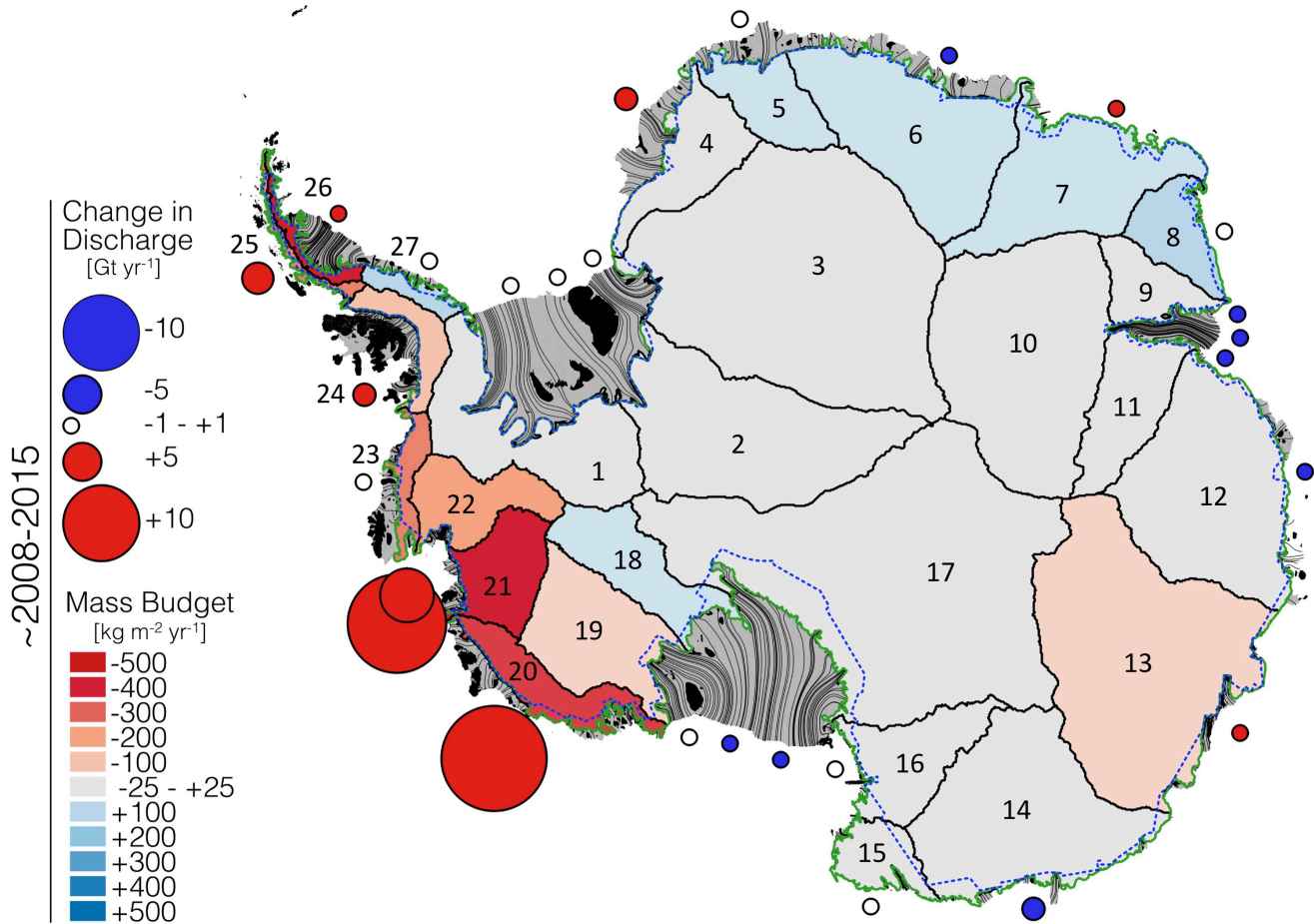
Figure 9: Mass budget and change in discharge for the 27 basins defined by Zwally et al. (2002). Mass budget is calculated as described in Table 2 using 2008-15 average surface mass balance in the main and inset figures, respectively. Change in discharges (circles) calculated by differencing the pan-Antarctic SAR mapping of Rignot et al. (2011a, circa-2008) with weighted average of all 2015 image pairs displacements supplemented with 2009 SAR velocities to fill missing Landsat coverage poleward of 82.5 degrees south (*Scheuchl et al.*, 2012) with a correction for acquisition time differences to provide an estimate of total discharge for the interior basins (2, 17 and 18; see Table 2). Flux gates FG1 and FG2 are shown with solid green and dashed blue lines respectively.

770

775   Tables:

Table 1: Data sources and percentages for radio-echo sounding data used to compile flux gates.

Data set	GL0	FGI	FG2	Reference
IceBridge MCoRDS-2	5.3 %	16.1 %	31.5 %	Leuschen et al. 2010
IceBridge HiCARS-2	2.1 %	5.4 %	20.2 %	Blankenship et al. 2012
CReSIS	0.4 %	0.3 %	0.3 %	Gogineni 2012
BAS-surveys	1.7 %	7.4 %	9.0 %	https://legacy.bas.ac.uk/data/aerogeo/
AADC-Amery	2.6 %	2.5 %	12.1 %	Allison and Hylland 2010
BELARE/AWI	0.1 %	2.4 %	4.1 %	Callens et al. 2014; 2015
Bedmap-2 data cell	6.9 %	8.3 %	18.3 %	Fretwell et al. 2013a
Sum	19.2 %	42.4%	95.6 %	

780 **Table 2: Surface area, cross sectional area for flux gate FG2, discharge corrected for dynamic volume change and surface mass balance between flux gate FG2 and the grounding line, basal melting, surface mass balance (SMB) and net mass balance for the 27 basins defined by Zwally et al. (2002). Cumulative numbers are provided for the East Antarctic Ice Sheet (EAIS: B2-17), the West Antarctic Ice Sheet (WAIS: B1, B18-23), and the Antarctic Peninsula (AP: B24-B27). Basal melt rates are from Van Liefferinge and Pattyn (2013) and calculated according to Pattyn (2010). SMB is calculated using the RACMO2.3 regional climate model at**
785 **5.5 km (*van Wessem et al.*, 2016) resolution over the Antarctic Peninsula and 27 km elsewhere (*van Wessem et al.*, 2014) and averaged over the 2008-2015 period. The net mass balance is calculated as the 2008-2015 SMB minus the average rate of discharge minus basal melt. Due to large and poorly constrained uncertainties in ice thickness and modeled SMB, net mass balance for Basins 25* and 26* are determined by updating the mass balance estimate of Scambos et al. 2014 with changes in discharge determined here (see Appendix B). Discharge for 2008 is derived from Rignot et al. (2011) and for 2015 from the mean of two JPL**
790 **2015 Landsat 8 velocity mappings (median and error weighted).**

basin	area km²	flux gate km²	discharge [Gt yr⁻¹] 2008	2015	Δ	basal melt Gt yr⁻¹	SMB [Gt yr⁻¹] 2008-15	net mass change Gt yr⁻¹	kg m⁻² yr⁻¹
1	474800	987 ± 53	110 ± 7	112 ± 7	2 ± 3	3 ± 0	121 ± 24	7 ± 25	15 ± 53
2	765400	305 ± 33	48 ± 6	47 ± 4	0 ± 4	3 ± 1	52 ± 10	2 ± 12	2 ± 16
3	1556600	213 ± 18	59 ± 4	60 ± 4	1 ± 2	5 ± 2	74 ± 15	9 ± 15	6 ± 10
4	241200	351 ± 55	41 ± 8	43 ± 7	2 ± 3	1 ± 0	45 ± 9	2 ± 12	8 ± 49
5	185300	196 ± 30	30 ± 5	31 ± 4	1 ± 2	1 ± 0	36 ± 7	5 ± 9	26 ± 47
6	607700	501 ± 59	60 ± 7	59 ± 6	-1 ± 3	3 ± 0	81 ± 16	17 ± 17	29 ± 29
7	492500	495 ± 62	67 ± 8	69 ± 8	2 ± 2	2 ± 0	93 ± 19	23 ± 20	47 ± 41
8	161200	277 ± 32	17 ± 3	18 ± 3	1 ± 2	1 ± 0	36 ± 7	18 ± 8	112 ± 50
9	146000	219 ± 18	17 ± 3	17 ± 2	-1 ± 2	1 ± 0	17 ± 3	0 ± 5	-2 ± 31
10	919300	55 ± 5	34 ± 4	33 ± 3	-1 ± 2	3 ± 1	42 ± 8	6 ± 9	6 ± 10
11	255200	187 ± 14	13 ± 3	12 ± 2	-1 ± 2	1 ± 1	16 ± 3	2 ± 4	6 ± 16
12	727100	610 ± 74	109 ± 11	108 ± 10	0 ± 3	5 ± 1	128 ± 26	14 ± 28	19 ± 38
13	1130800	667 ± 50	225 ± 18	223 ± 17	-2 ± 5	7 ± 1	201 ± 40	-30 ± 44	-26 ± 39
14	718500	714 ± 48	129 ± 10	129 ± 9	-1 ± 3	5 ± 1	125 ± 25	-9 ± 27	-12 ± 37
15	123800	190 ± 11	26 ± 6	26 ± 5	0 ± 2	1 ± 0	25 ± 5	-2 ± 8	-12 ± 61
16	262000	159 ± 13	13 ± 2	14 ± 2	0 ± 2	1 ± 0	10 ± 2	-5 ± 3	-18 ± 12
17	1825800	646 ± 51	67 ± 8	67 ± 7	0 ± 3	5 ± 2	78 ± 16	6 ± 17	3 ± 10
18	261400	125 ± 16	9 ± 3	8 ± 2	-1 ± 2	2 ± 1	23 ± 5	13 ± 5	49 ± 21
19	367700	258 ± 34	44 ± 6	45 ± 6	1 ± 2	3 ± 1	37 ± 7	-11 ± 10	-30 ± 26
20	180100	490 ± 54	170 ± 14	182 ± 14	11 ± 4	2 ± 0	112 ± 22	-67 ± 27	-371 ± 147
21	207500	179 ± 12	180 ± 12	190 ± 11	10 ± 4	2 ± 1	98 ± 20	-89 ± 23	-429 ± 111
22	210200	112 ± 7	127 ± 8	134 ± 8	7 ± 2	2 ± 0	84 ± 17	-49 ± 19	-231 ± 89
23	74600	249 ± 20	82 ± 7	82 ± 7	0 ± 3	1 ± 0	65 ± 13	-18 ± 15	-240 ± 202
24	100600	211 ± 15	94 ± 7	95 ± 6	2 ± 3	1 ± 0	86 ± 17	-9 ± 19	-93 ± 185
25*	*34700*	*78 ± 15*	*88 ± 13*	*91 ± 12*	*4 ± 5*	*0 ± 0*	*100 ± 20*	*-10 ± 21*	*-297 ± 605*
26*	*42000*	*116 ± 12*	*23 ± 4*	*25 ± 3*	*2 ± 2*	*1 ± 0*	*29 ± 6*	*-17 ± 7*	*-405 ± 174*
27	52000	89 ± 9	12 ± 3	12 ± 2	0 ± 2	0 ± 0	18 ± 4	6 ± 5	112 ± 88
EAIS	10118500	5786 ± 165	956 ± 30	955 ± 28	-1 ± 11	45 ± 4	1058 ± 66	58 ± 73	6 ± 7
WAIS	1776200	2400 ± 88	723 ± 24	753 ± 22	29 ± 8	16 ± 1	541 ± 45	-213 ± 51	-120 ± 29
AP	*229200*	*493 ± 26*	*218 ± 15*	*224 ± 14*	*7 ± 6*	*2 ± 0*	*234 ± 27*	*-31 ± 29*	*-135 ± 128*
All	**12123900**	**8679 ± 189**	**1897 ± 41**	**1932 ± 38**	**35 ± 15**	**63 ± 4**	**1834 ± 84**	**-186 ± 93**	**-15 ± 8**

Appendix A: Uncertainty Quantification

1.1A Ice Discharge

795 The uncertainty in flux estimates were calculated for each of the 27 basins as:

$$\sigma F = \sqrt{\sigma F_H{}^2 + \sigma F_{dH}{}^2 + \sigma F_V{}^2 + \sigma F_{\bar{V}}{}^2 + \sigma F_{SMB}{}^2 + \sigma F_{dV_{dyn}/dt}{}^2}$$

where σF_H is due to uncertainties in ice-equivalent thickness, σF_{dH} is due to uncertainties in the change of ice-equivalent thickness between the measurement times of ice thickness and surface velocity, σF_V is due to uncertainties in measured

800 velocity, an $\sigma F_{\bar{V}}$ is due to the assumption that the depth averaged velocity ($\bar{V}$) is equal to the surface velocity. $\sigma F_{dV_{dyn}/dt}$ and σF_{SMB} are uncertainties introduced by dynamic volume change and surface mass balance corrections applied between the flux gate the true grounding line. $\sigma F_{dV_{dyn}/dt}$ was taken to be 0.1 m yr^{-1} for surfaces moving faster than 200 m yr^{-1}. σF_{SMB} was taken to be 20% of the SMB. Uncertainties in flux resulting from uncertainties in ice thickness, changes in ice thickness and surface velocity were propagated assuming a conservative correlation length along the flux gate as follows:

805

$$\sigma F_H = \sqrt{\sum_1^{n_H} \left(\sum_{i=1}^{m_H} \sigma H_i W_i V_i \right)^2}$$

$$\sigma F_{dH} = \sqrt{\sum_1^{n_{dH}} \left(\sum_{i=1}^{m_{dH}} \sigma \frac{dH}{dt}_i dt_i W_i V_i \right)^2}$$

$$\sigma F_V = \sqrt{\sum_1^{n_V} \left(\sum_{i=1}^{m_V} \sigma V_i W_i H_i \right)^2 + \sum_{i=1}^{nn} \sigma V_{0i} W_i H_i}$$

810

Where m is the number of point estimates of flux (x) for each correlation length distance along the flux gate and n is the number of discrete uncorrelated lengths for each basin for measurements of ice thickness (H), changes in ice thickness (dH) and the surface velocity normal to the flux gate (V). Uncertainties in ice thickness (σH_i) are taken as the RSS of the thickness estimate and the FAC. Uncertainties in changes in ice thickness ($\sigma \frac{dH}{dt}$) are determined as the RSS of uncertainty

815   due to changes in FAC and surface elevation. dt is the difference in time between the measurement of ice thickness and the

measurement of surface velocity. σF_V is modeled using a velocity uncertainty component σV_0 that is fully correlated at

lengths smaller than an estimated correlation length and uncorrelated at larger lengths (σV). Comparing Landsat and SAR

velocities measured at flux gate nodes for basins with minimal change in ice discharge (B1-19 & B27), i.e. where velocity

differences are assumed to be indicative measurement uncertainty, we were able to model the observed RMSE between

820   Landsat and SAR observations (Figure A2) setting $\sigma V_0 = 3$ m yr^{-1} and $\sigma V = 1$ m yr^{-1} with a correlation length of 1000 km

for both the SAR and Landsat mappings. Uncertainties in velocities can be as high as 20-30 m yr^{-1} locally but are largely

uncorrelated at basin scales. There is insufficient data to determine rigorous estimates of the correlation lengths for ice

thickness, change in ice thickness, and surface velocity, all of which are likely spatially variable. Instead we took a

conservative approach and assigned a correlation length of 1000 km to all three measurements.

825
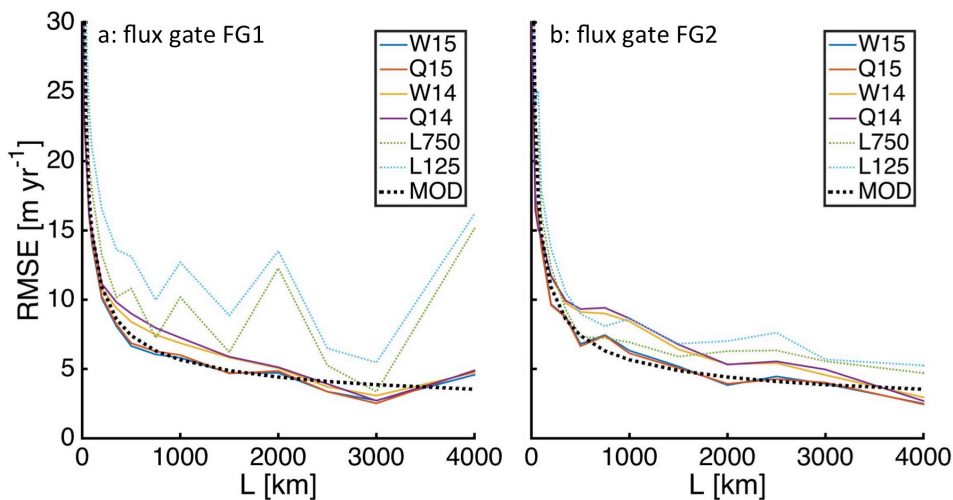
Figure A2: RMSE of the Landsat component of velocity that is normal to the flux gate cross section at FG1 (a) and FG2 (b) flux nodes relative to ~2008 SAR velocities (Rignot et al., 2011) as a function of averaging distance (L). MOD is the modeled uncertainty assuming a fully-correlated uncertainty of 1 m yr^{-1} plus a 3 m yr^{-1} uncertainty that is uncorrelated at distances greater
830   **than 1000 km.**

When calculating ice flux we assumed that the surface velocity was equal to the depth-averaged velocity. This approach

neglects vertical gradients in ice velocity that result from the stress-dependent plastic deformation (creep) of ice. Since

surface velocities are always larger than the depth averaged velocity this introduced a positive bias into our estimates of ice

835   flux. Neglecting sliding and assuming a depth constant creep parameter (A) the depth-averaged velocity is 80% of the

surface velocity (*Cuffey and Paterson*, 2010). Assuming parallel flow and a linear increase in shear stress with depth, the

surface velocity due to creep (Vs) can be calculated as follows:

$$Vs = \frac{2A}{1+n} t_b^n H$$

840 where n is the creep exponent, H is the ice thickness, and t_b is the driving stress at the bed. n is typically assumed to be 3 and so is done here. t_b is calculated using the surface slope and ice depth (*Cuffey and Paterson*, 2010). The creep parameter A (Figure A3a) is taken from Ice Sheet System Model (ISSM) output generated as part of the Sea-level Response to Ice Sheet Evolution (SeaRISE) experiments (*Bindschadler et al.*, 2013). We calculated surface slope from a CryoSat-2 DEM that was smoothed at a scale of several times the ice thickness (20 km). Ice thickness was taken from Bedmap-2 (*Fretwell et*

845 *al.*, 2013b). Vs varied between 0 m yr^{-1} at the ice divides to 10 m yr^{-1} in steeply sloped outlet glaciers near the coast (Figure A3b). We considered 20% of V_s to be the upper bound of the bias introduced into our flux estimates due to vertical gradients in the velocity field ($\sigma F_{\overline{V}}$), calculated as:

$$\sigma F_{\overline{V}} = 0.2 \sum_{x=1}^{nn} Vs_i W_i H_i$$

850 where nn is the number nodes along the basin flux gate. This is an upper bound scenario, as A increases rapidly with temperature, and ice sheet temperature is typically at a maximum near the bed. This results in a higher concentration of shear deformation near the base of the ice sheet than inferred from a depth-constant A.

Uncertainties in flux estimates were assumed to be uncorrelated between basins.

855
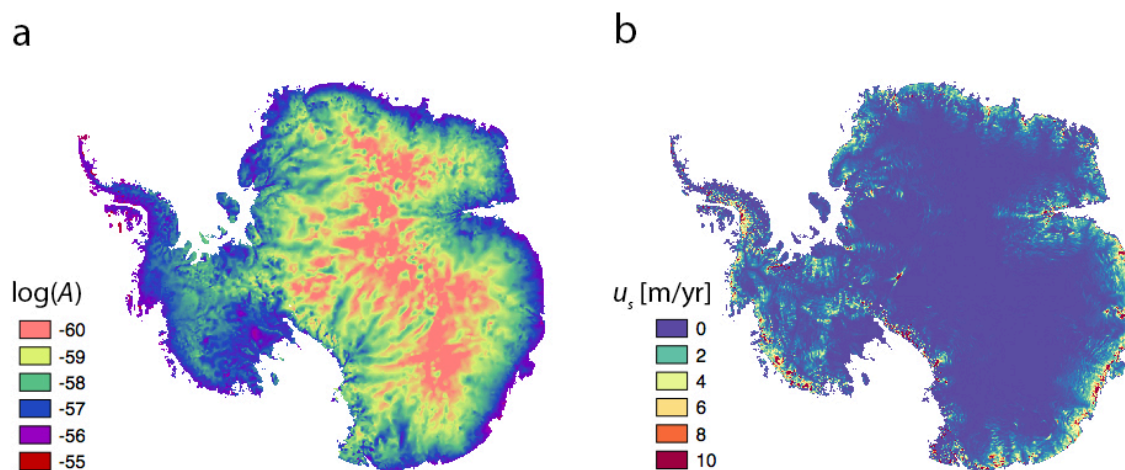
Figure A3: Creep parameter (A: s^{-1} Pa^{-3}) shown in log scale (a). Estimated surface velocity due to ice creep (U_s).

1.2A Change in Ice Discharge

Uncertainty in flux-change estimates (σdF) are calculated as:

860

$$\sigma dF = \sqrt{\sigma dF_H{}^2 + \sigma dF_{dH}{}^2 + \sigma dF_V{}^2 + \sigma dF_{no\_data}{}^2}$$

where σdF_H is the thickness-related uncertainty and is calculated as:

$$\sigma dF_H = \sigma F_{H0}\frac{dF}{F}$$

865   where dF is the change in flux and F is the total flux. σdF_{dH} is calculated in the same way as σF_{dH} but setting dt to the time separation between repeat measurements of velocity. σdF_v is the flux-change uncertainty from the measured velocity and is determined as:

$$\sigma dF_v = \sqrt{\sigma F_{v1}{}^2 + \sigma dF_{v2}{}^2}$$

870   where σF_v is the uncertainty in flux introduced from uncertainties in surface velocity for two measurement epochs (1 & 2). σdF_{no_data} is the flux-change uncertainty introduced by the assumption of zero change in flux for areas lacking reliable repeat measurements (σF_{no_data}) and for areas between the flux gate and the grounding line (σF_{SMB}) and is calculated as:

$$\sigma dF_{no\_data} = 0.1\big(\sigma F_{SMB} + \sigma F_{no\_data}\big)$$

875   Uncertainties   in   flux   change   estimates   were   assumed   to   be   uncorrelated   between   basins.

Appendix B: Northern Antarctic Peninsula Net Mass Balance

Narrow deep fjords and steep spatial and temporal gradients in surface mass balance for the North Antarctic Peninsula (B25-26) introduced large and poorly characterized uncertainties into estimates of ice discharge and $\sigma F_{dv/dt}$ that propagated to highly uncertain estimates of net mass change. For this reason, we derived our estimates of net mass change using previously

880 published estimates from repeat surface elevation measurements that we added to our estimates of change in ice discharge. Work by Scambos et al. (2014), based on elevation changes and recent gravity work (*Harig and Simons*, 2015), suggest that the northern Antarctic Peninsula region (precise study extents vary) has seen continued mass losses at more or less a constant rate of 25-30 Gt yr^{-1} for the period 2003-2015; this is further supported by examination of JPL mascon (*Watkins et al.*, 2015) mass anomalies and RACMO surface mass budget anomalies (See Figure B1). Estimates based on CryoSat-2

885 (*McMillan et al.*, 2014) suggest a reduced mass loss for B25 and B26 (below the significance level) for the period 2010-2013, but usable data from CryoSat-2 for this rugged region are sparse.
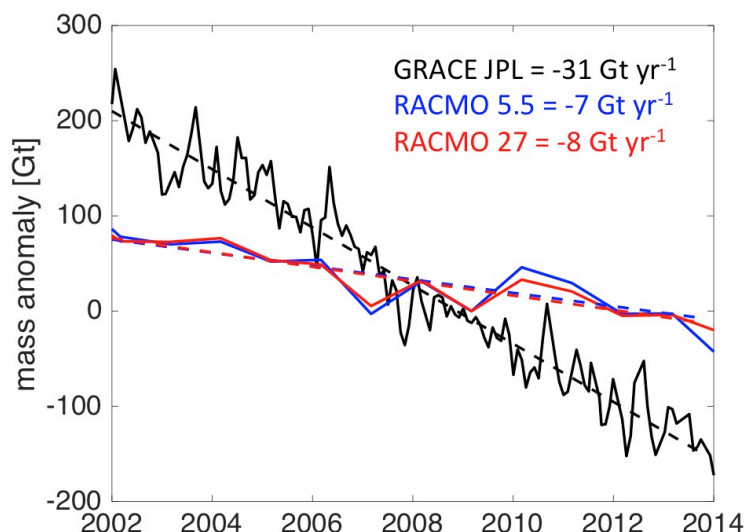
Figure B1: Rates of 2002-2014 mass change as derived from linear fits to cumulative anomalies of RACMO surface mass balance
890 **determined at 5.5 km (blue line) and 27 km (red line), and JPL V2.0 mascon anomalies (black line: grace.jpl.nasa.gov/data/get-data/jpl_global_mascons/) for the North Antarctic Peninsula. Surface mass balance and JPL mascon anomalies were integrated for the the 7 mascons overlapping the Northern Antarctic Peninsula (4324, 4325, 4372, 4373, 4374, 4415, 4416). For plotting purposes the surface mass balance anomalies were determined relative to the 1979-2003 mean. JPL mascons are corrected for changes in solid earth using the glacial isostatic adjustment (GIA) correction modeled by Geruo A and John Wahr.** *This figure is*
895 *provided to support the argument for a relatively steady rate of North Antarctic Peninsula mass change between the 2003 and 2015 and not to support the magnitude of that change which is sensitive to the choice of the model used for the GIA correction.*

To estimate the net mass balance for basins B25 and B26, we used estimates of glacier mass loss determined from repeat elevation measurements for the 2003-2011 period as a starting point (*Scambos et al.*, 2014). Since this study was restricted to
900 areas north of 66°S, we added our estimate of change in ice discharge south of 66°S (6 Gt yr^{-1}: Table 2) to estimate the basin-

wide net mass balances for 2008-2015. The uncertainty in the net budget was calculated as the RSS of the uncertainty in the basin estimate of change in discharge, the uncertainty in the net balance estimated in Scambos et al. (2014), and the uncertainty in the surface mass budget. Basin totals and uncertainties are provided in Table 2.